

# Three-dimensional convection of an infinite-Prandtl-number compressible fluid in a basally heated spherical shell

By DAVID BERCOVICI<sup>1</sup>, GERALD SCHUBERT<sup>2</sup>  
AND GARY A. GLATZMAIER<sup>3</sup>

<sup>1</sup>Department of Geology and Geophysics, School of Ocean and Earth Science and Technology,  
University of Hawaii, Honolulu, HI 96822, USA

<sup>2</sup>Department of Earth and Space Sciences, University of California, Los Angeles,  
CA 90024, USA

<sup>3</sup>Earth and Environmental Sciences Division, Los Alamos National Laboratory,  
NM 87545, USA

(Received 10 November 1989 and in revised form 13 December 1991)

A numerical investigation is made of the effects of compressibility on three-dimensional thermal convection in a basally heated, highly viscous fluid spherical shell with an inner to outer radius ratio of approximately 0.55, characteristic of the Earth's whole mantle. Compressibility is implemented with the anelastic approximation and a hydrostatic adiabatic reference state whose bulk modulus is a linear function of pressure. The compressibilities studied range from Boussinesq cases to compressibilities typical of the Earth's whole mantle. Compressibility has little effect on the spatial structure of steady convection when the superadiabatic temperature drop across the shell  $\Delta T_{sa}$  is comparable to a characteristic adiabatic temperature. When  $\Delta T_{sa}$  is approximately an order of magnitude smaller than the adiabatic temperature, compressibility is significant. For all the non-Boussinesq cases, the regular polyhedral convective patterns that exist at large  $\Delta T_{sa}$  break down at small  $\Delta T_{sa}$  into highly irregular patterns; as  $\Delta T_{sa}$  decreases convection becomes penetrative in the upper portion of the shell and is strongly time dependent at Rayleigh numbers only ten times the critical Rayleigh number,  $\langle Ra \rangle_{cr}$ . Viscous heating in the compressible solutions is concentrated around the upwelling plumes and is greatest near the top and bottom of the shell. Solutions with regular patterns (and large  $\Delta T_{sa}$ ) remain steady up to fairly high Rayleigh numbers ( $100 \langle Ra \rangle_{cr}$ ), while solutions with irregular convective patterns are time dependent at similar Rayleigh numbers. Compressibility affects the pattern evolution of the irregular solutions, producing fewer upwelling plumes with increasing compressibility.

---

## 1. Introduction

Convective flow in the Earth's mantle has been the subject of extensive research because of its relevance to plate tectonics and the structure and evolution of the terrestrial planets (Oxburgh & Turcotte 1978; Schubert 1979; Schubert, Stevenson & Stevenson & Cassen 1980; Olson, Silver & Carlson 1990). Evidence for convection exists in the directly measurable motions of the tectonic plates at the Earth's surface (Minster & Jordan 1978, 1987; Kroger *et al.* 1987), and in the correlations of seismically and gravitationally inferred mantle heterogeneities and core-mantle boundary topography with tectonic features (Runcorn 1967; Dziewonski 1984;

Woodhouse & Dziewonski 1984; Hager *et al.* 1985; Dziewonski & Woodhouse 1987; Silver, Carlson & Olson 1988). Subsolidus convection in the mantles of the other terrestrial planets is largely inferred from tectonic and volcanic features on the surfaces of the planets and relatively sparse gravity measurements (Schubert 1979; Kaula 1990).

Since the whole mantle thicknesses of Venus, Earth and Mars are between 45 and 50% of the mean planetary radius (Stevenson, Spohn & Schubert 1983) global models of mantle convection require a spherical geometry (see Roberts 1987). Analytic investigations of convection in spherical shells have been performed with perturbation methods to determine the horizontal patterns of steady three-dimensional flow (Busse 1975; Busse & Riahi 1982, 1988), and mean field techniques to examine heat flow characteristics (Olson 1981; Quarenì & Yuen 1988). However, strongly nonlinear solutions to the fluid dynamical equations are only attainable through experimentation. A limited number of laboratory experiments – whose difficulty is compounded by the need for a local central gravity field – have been performed (Hart, Glatzmaier & Toomre 1986*a*; Hart *et al.* 1986*b*), while the considerably more facile numerical experimentation has been relatively extensive. However, most numerical work has been for axisymmetric spherical shells (Hsui, Turcotte & Torrance 1972; Zebib, Schubert & Straus 1980; Schubert & Zebib 1980; Zebib *et al.* 1983; Zebib, Goyal & Schubert 1985; Machetel & Rabinowicz 1985; Machetel & Yuen 1986, 1987, 1988, 1989; Bercovici, Schubert & Zebib 1988) and/or for low Rayleigh numbers (a non-dimensional measure of the vigour of convection) (Young 1974; Machetel, Rabinowicz & Bernadet 1986). The accessibility of supercomputers in recent years has made three-dimensional studies of spherical convection at high Rayleigh numbers more realizable (Baumgardner 1985, 1988; Glatzmaier 1988; Bercovici *et al.* 1989*c*; Bercovici, Schubert & Glatzmaier 1989*a, b*; Schubert, Bercovici & Glatzmaier 1990; Glatzmaier, Schubert & Bercovici 1990; Bercovici, Schubert & Glatzmaier 1991). Spherical geometry and three-dimensionality have been shown to be important in possibly accounting for some of the major tectonic features at the Earth's surface (Bercovici *et al.* 1989*a*).

Mantle convection has generally been modelled in the Boussinesq limit. However, for a large planet with a thick mantle, compressibility can be significant. For the Earth, the density of silicates increases by 60% from the top of the mantle to the bottom (taking into account phase and/or compositional changes) (Stacey 1977; Dziewonski & Anderson 1981). The effects of compressibility have been considered in two-dimensional studies of convective flow (Peltier 1972; Turcotte *et al.* 1974; Graham 1975; Hewitt, McKenzie & Weiss 1975; Jarvis & McKenzie 1980; Steinbach, Hansen & Ebel 1989; Machetel & Yuen 1989; Solheim & Peltier 1990). While the specific nature (e.g. time-dependence, radial structure) of the convective solutions has been found to be influenced by compressibility, the overall heat transport and horizontally averaged temperature profiles merely reflect the superposition of an adiabat on essentially Boussinesq solutions. However, compressibility introduces additional nonlinearities (e.g. viscous heating) into the convective equations which influence both the temporal evolution and the spatial symmetry of the convective solutions. Since the nonlinearities of the Boussinesq equations break the axisymmetry of the marginally stable state into three-dimensional patterns with regular polyhedral symmetry (Busse 1975; Busse & Riahi 1982), any further symmetry breaking induced by additional nonlinearities must occur in three dimensions. Therefore, an investigation of the influence of compressibility on convection should account for three-dimensional effects.

In this paper, we present a numerical investigation of convection in a basally heated spherical shell characteristic of the Earth's whole mantle for the range of compressibilities pertinent to the terrestrial mantles. We investigate the effects of three parameters that we believe to have the greatest bearing on mantle convection. These parameters are the Rayleigh number, the dissipation number (a non-dimensional measure of compressibility), and the ratio  $\bar{T}_{\text{bot}}/\Delta T_{\text{sa}}$  ( $\bar{T}_{\text{bot}}$  is the adiabatic reference temperature at the shell's base, and  $\Delta T_{\text{sa}}$  is the superadiabatic temperature drop across the shell). The parameter  $\bar{T}_{\text{bot}}/\Delta T_{\text{sa}}$  partially controls the superadiabaticity of the fluid. This parameter has not previously been varied in investigations of compressible convection, yet compressibility has its greatest effects when  $\bar{T}_{\text{bot}}/\Delta T_{\text{sa}}$  is large.

The following sections of this paper describe the theory of compressible convection, the computational model used for the numerical experiments, a verification of the model, a linear stability analysis for the parameter range of this study, and results of the experiments for both low- and high-Rayleigh-number solutions.

## 2. The theory of compressible convection

The model equations for subsonic compressible flow employ the anelastic approximation (Gough 1969); i.e. mass flux is solenoidal. Terrestrial mantle material is extremely viscous, thus the infinite-Prandtl-number  $Pr = \nu/\kappa$  (where  $\nu$  is kinematic viscosity and  $\kappa$  is thermal diffusivity) approximation is used. With these assumptions, the equations of mass, momentum and energy conservation (or entropy transport) are

$$\nabla \cdot (\bar{\rho} \mathbf{v}) = 0, \quad (2.1)$$

$$0 = -\nabla P' + \nabla \cdot \boldsymbol{\sigma} - \rho' g \mathbf{f}, \quad (2.2)$$

$$\bar{\rho} \bar{T} \left( \frac{\partial S'}{\partial t} + \mathbf{v} \cdot \nabla S' \right) = \nabla \cdot (k \nabla (\bar{T} + T')) + Q + \boldsymbol{\sigma} : \dot{\boldsymbol{\epsilon}}, \quad (2.3)$$

where  $\rho$ ,  $T$ ,  $P$  and  $S$  are density, temperature, pressure and entropy, respectively; barred quantities refer to a spherically symmetric adiabatic hydrostatic reference state and primed quantities are perturbations to that state. The adiabatic reference state simply defines a typical, average adiabat; very little of the adiabatically rising or sinking fluid actually passes along this adiabat, but moves instead along either a hotter (for warm rising fluid) or colder (cold sinking fluid) adiabat. A linear equation of state for the perturbation quantities is derived by carrying out a first-order Taylor series expansion of the variables around their adiabatic values. Thus, given entropy and pressure perturbations to the reference state  $S'$  and  $P'$ , the temperature and density perturbations are, respectively,

$$T' = \left( \frac{\partial T}{\partial S} \right)_P S' + \left( \frac{\partial T}{\partial P} \right)_S P' = \bar{T} \left( \frac{1}{c_p} S' + \frac{\gamma}{K_s} P' \right), \quad (2.4)$$

$$\rho' = \left( \frac{\partial \rho}{\partial S} \right)_P S' + \left( \frac{\partial \rho}{\partial P} \right)_S P' = \bar{\rho} \left( -\frac{\alpha \bar{T}}{c_p} S' + \frac{1}{K_s} P' \right), \quad (2.5)$$

where  $\alpha$  is thermal expansivity,  $c_p$  is the specific heat at constant pressure,  $K_s$  is the bulk modulus (i.e. adiabatic incompressibility) and

$$\gamma = \frac{d \ln \bar{T}}{d \ln \bar{\rho}} = \frac{\alpha K_s}{\bar{\rho} c_p}$$

is the Grüneisen parameter. The deviatoric stress tensor is  $\sigma = 2\eta(\dot{\epsilon} - \frac{1}{3}(\nabla \cdot \mathbf{v})I)$  and the strain rate tensor is  $\dot{\epsilon} = \frac{1}{2}(\nabla \mathbf{v} + [\nabla \mathbf{v}]^t)$ , where  $\mathbf{v}$  is the velocity vector,  $I$  is the identity matrix, and  $\eta$  is the dynamic viscosity ( $\eta = \bar{\rho}\nu$ ). The volumetric internal heating rate  $Q$  is zero in this study. Gravity  $g$  is a function of radius  $r$  only ( $\hat{r}$  is the radial unit vector), and  $k$  is the thermal conductivity ( $k = \bar{\rho}c_p\kappa$ ).

The linear equation of state (2.4) is a good approximation if  $T'/\bar{T} \ll 1$  or if  $c_p$  is proportional to  $T$ . However, in this study,  $c_p$  is assumed constant although  $T'/\bar{T}$  is not necessarily  $\ll 1$ ; this is a necessary inconsistency to provide simple closure of the model. Such inconsistencies are often adopted – sometimes inadvertently – in compressible models of convection; e.g. the exact differential  $dS(T, P)$  used in other formulations (e.g. Jarvis & McKenzie 1980; Machetel & Yuen 1989; Solheim & Peltier 1990) to expand  $DS/Dt$  in terms of  $T$  and  $P$  has an implied Maxwell relation that constrains  $\alpha \sim 1/T$  (if  $c_p$  is constant), whereas  $\alpha$  is assumed constant or a simple function of radius. The results presented later in this paper are *a posteriori* evidence that the linear equation of state does not present a serious inconsistency: when the linear equation of state is the poorest approximation (i.e. when  $T'/\bar{T}$  is not  $\ll 1$ ), compressibility has very little effect. Thus, non-Boussinesq effects that are potentially inconsistently calculated because of the linear equation of state are negligible when the linear equation of state is least accurate. (Boussinesq effects are fully represented with the above equations; i.e. the Boussinesq equations are completely recovered when there is no density or temperature stratification.) Although this finding may be affected by the linear equation of state, it makes intuitive sense; i.e. when  $T'/\bar{T} \sim O(1)$ , thermal anomalies caused by viscous heating and the stabilizing effects of stratification are overwhelmed by the large imposed superadiabatic temperatures. Furthermore, (2.4) is weakest at representing the relation between  $S'$  and  $T'$  when  $T'/\bar{T}$  is not  $\ll 1$ . However, the leading-order effect should be that  $S'$  and  $T'$  monotonically increase with one another (since more heating causes temperature to increase); i.e.  $S'$  and  $T'$  should be odd functions of each other. Thus it is unlikely that a second-order correction to (2.4) (in which  $S'$  and  $T'$  are even functions of one another) would – or should – be very significant. The most important correction to (2.4) is probably of third order, thus corrections to the linear equation of state may be smaller than what might be expected. Finally, it can be shown, for a linear equation of state and constant heat capacity, that the coefficient of the material derivative of  $S'$  on the right-hand side of (2.3) is  $\bar{\rho}\bar{T}$  instead of  $\rho T$  (Bercovici 1989).

Equation (2.2) does not include the effects of the perturbation gravitational potential which cannot be absorbed into the isotropic stress (i.e. the pressure) as in the Boussinesq approximation. This effect was considered in a previous study (Glatzmaier 1988) and was found to make no more than a 5% difference in the solutions. The effect may be even smaller since that study did not include the contribution of surface masses that arise from dynamic topography.

The validity of the anelastic approximation requires  $\rho' \ll \rho$  (or  $\bar{\rho}$ ). Density perturbations due to pressure perturbations  $P'$  are related to  $\rho'$  by  $\rho' \sim P'/c^2$  (where  $c$  is the sound speed). In low-Prandtl-number flow,  $P' \sim \rho u^2$  (where  $u$  is a characteristic velocity), and thus  $\rho'/\rho \sim M^2$ , where  $M \equiv u/c$  is the Mach number (Batchelor 1967; Gough 1969). However, in infinite-Prandtl-number flow, a pressure perturbation  $P'$  is balanced by a viscous stress of characteristic magnitude  $\eta u/L$  (where  $L$  is a characteristic lengthscale); therefore,  $\rho'/\rho \sim M^2/Re$  (where  $Re \equiv \rho u L/\eta$  is the Reynolds number). Previous studies of infinite- $Pr$  compressible convection have justified the anelastic approximation by noting that for the Earth's mantle,

$M^2 \sim 10^{-25}$  (Jarvis & McKenzie 1980; Glatzmaier 1988; Machetel & Yuen 1989; Bercovici *et al.* 1989*a, b, c*; Solheim & Peltier 1990). However, the validity of the anelastic approximation for mantle convection actually rests on the fact that  $M^2/Re \sim 10^{-5}$ , which although small is not nearly as small as  $M^2$ .

In this paper, the ratio  $\bar{T}_{\text{bot}}/\Delta T_{\text{sa}}$  is a variable parameter, defined in §1. (In a planetary mantle,  $\bar{T}_{\text{bot}}$  is the temperature of the mantle adiabat extrapolated down to the base of the mantle and  $\Delta T_{\text{sa}}$  is essentially the sum of the temperature drops across the thermal boundary layers.) This parameter partially controls the degree of superadiabaticity of the fluid. For example, in a hydrostatic state, the entropy gradient is

$$\frac{dS}{dr} = \frac{c_p}{T} \left( \frac{dT}{dr} + \frac{\alpha g T'}{c_p} \right) = \frac{c_p}{T} \left( \frac{dT}{dr} - \left( \frac{dT}{dr} \right)_S \right) \quad (2.6a)$$

(where  $(d/dr)_S$  is the radial derivative at constant entropy). If we make the substitutions

$$\left( \frac{dT}{dr} \right)_S = \frac{d\bar{T}}{dr}, \quad \bar{T} = \bar{T}_{\text{bot}} a(r)$$

where  $a(r_{\text{bot}}) = 1$  and  $(da/dr) < 0$ ) and

$$\frac{dT}{dr} = - \frac{\Delta T f(r)}{d}$$

(where  $\Delta T = \Delta T_{\text{sa}} + \bar{T}_{\text{bot}} - \bar{T}_{\text{top}}$  is the total temperature drop,  $d$  is the shell thickness and  $f$  is a function of radius, e.g.  $f(r) = r_{\text{top}} r_{\text{bot}}/r^2$  when the layer is conductive), then

$$\frac{dS}{dr} = \frac{c_p \Delta T_{\text{sa}}}{T d} \left\{ -f(r) + \frac{\bar{T}_{\text{bot}}}{\Delta T_{\text{sa}}} \left( \left| \frac{da}{dr} \right| d - [1 - a(r_{\text{top}})] f(r) \right) \right\}. \quad (2.6b)$$

The fluid is subadiabatic or adiabatic ( $dS/dr \geq 0$ ) when the term proportional to  $\bar{T}_{\text{bot}}/\Delta T_{\text{sa}}$  is positive and large relative to  $f(r)$ . Thus the parameter  $\bar{T}_{\text{bot}}/\Delta T_{\text{sa}}$  partially controls the degree of super- or subadiabaticity.

In this study  $\eta$ ,  $k$ ,  $\gamma$  and  $c_p$  are assumed constant. Thus, to non-dimensionalize equations (2.1)–(2.4) (with (2.5) substituted into (2.2)), we nondimensionalize time by  $\bar{\rho}_{\text{bot}} c_p d^2/k$  (where  $\bar{\rho}_{\text{bot}}$  is the density of the reference state at the base of the shell), distance by  $d$ , pressure and stress by  $\eta k / (\bar{\rho}_{\text{bot}} c_p d^2)$ , entropy by  $c_p \Delta T_{\text{sa}} / \bar{T}_{\text{bot}}$ , and the temperature perturbation by  $\Delta T_{\text{sa}}$  to obtain

$$\nabla \cdot \mathbf{v} = \frac{Di}{\gamma} v_r, \quad (2.7)$$

$$0 = -\nabla P' + \nabla^2 \mathbf{v} + \frac{1}{3} \nabla \left( \frac{Di}{\gamma} v_r \right) + \frac{\bar{\rho}_{\text{bot}} \bar{T}}{\bar{\rho} \bar{T}_{\text{bot}}} Ra S' \hat{\mathbf{r}} - \frac{Di}{\gamma} P' \hat{\mathbf{r}}, \quad (2.8)$$

$$\frac{\bar{\rho} \bar{T}}{\bar{\rho}_{\text{bot}} \bar{T}_{\text{bot}}} \frac{DS'}{Dt} = \nabla^2 \left( \frac{\bar{T}}{\Delta T_{\text{sa}}} + T' \right) + \left( \frac{\bar{\rho}}{\bar{\rho}_{\text{bot}}} \right)^2 \frac{Di}{Ra} \boldsymbol{\sigma} : \dot{\boldsymbol{\epsilon}}, \quad (2.9)$$

where

$$T' = \frac{\bar{T}}{\bar{T}_{\text{bot}}} S' + \alpha \bar{T} \frac{\bar{\rho}}{\bar{\rho}_{\text{bot}}} \frac{Di}{Ra} P'. \quad (2.10)$$

The Rayleigh number  $Ra = g \alpha \Delta T_{\text{sa}} d^3 / (\nu \kappa)$  and the dissipation number  $Di = \alpha g d / c_p$  can both be functions of radius. Although  $Di$  represents stratification due to compression (it is the ratio of shell thickness to the adiabatic temperature scale

height), the parameter  $Di/Ra$  is the ratio of flow-induced heating (e.g. viscous heating) to the heating supplied by the energy source, which, in this paper, is a hotter underlying core. The Boussinesq equations are exactly recoverable when  $Di = 0$  (if  $\gamma \neq 0$ ).

### 3. The numerical model

#### 3.1. The reference-state equations

The reference state of this study's model is based on the Murnaghan equation (Murnaghan 1951; Glatzmaier 1988) in which the bulk modulus  $K_s$  is a linear function of the reference-state pressure

$$\bar{\rho} \left( \frac{d\bar{P}}{d\bar{\rho}} \right)_s = K_s = K_0 + K' \bar{P}. \quad (3.1)$$

Equation (3.1) describes only the adiabat defined by  $\bar{P}$  and  $\bar{\rho}$ ; neighbouring adiabats are treated as perturbations to this one. With (3.1), the substitution  $\bar{\rho} = \bar{\rho}_{\text{bot}} \Theta^n$  and non-dimensionalization of  $r$  by  $d$ , the hydrostatic equation becomes the dimensionless Lane–Emden equation (Glatzmaier 1988)

$$\frac{d^2 \Theta}{dr^2} + \frac{2}{r} \frac{d\Theta}{dr} = - \frac{d^2}{R^2} \Theta^n, \quad (3.2)$$

where

$$R^2 = \frac{nK_0}{4\pi G \bar{\rho}_{\text{bot}} \bar{\rho}_{\text{top}}} \left( \frac{\bar{\rho}_{\text{bot}}}{\bar{\rho}_{\text{top}}} \right)^{1/n},$$

$\bar{\rho}_{\text{top}}$  is  $\bar{\rho}$  at  $r = r_{\text{top}}$ ,  $\Theta$  is the Lane–Emden function (Chandrasekhar 1939; Glatzmaier 1988), and  $n = 1/(K' - 1)$  is the polytropic index. The boundary conditions on density and gravity at the base of the shell require that

$$\Theta(r_{\text{bot}}) = 1, \quad (3.3)$$

$$\left. \frac{d\Theta}{dr} \right|_{r_{\text{bot}}} = \frac{-g_{\text{bot}}}{4\pi G \bar{\rho}_{\text{bot}} d} \left( \frac{d^2}{R^2} \right), \quad (3.4)$$

where  $g_{\text{bot}} = GM_{\text{core}}/r_{\text{bot}}^2$  ( $M_{\text{core}}$  is the mass of the underlying core). We constrain  $d^2/R^2$  by requiring that

$$\Theta(r_{\text{top}}) = \left( \frac{\bar{\rho}_{\text{top}}}{\bar{\rho}_{\text{bot}}} \right)^{1/n} \quad (3.5)$$

at  $r = r_{\text{top}}$ . The solutions for  $\Theta$  and  $d\Theta/dr$  together define the reference state. The adiabatic reference-state temperature is  $\bar{T} = \bar{T}_{\text{bot}} \Theta^{\gamma n}$ . Thermal expansivity  $\alpha$  is a function of radius (unless  $K' = 1$ ).

In summary, the non-dimensional parameters that define the reference state are  $K'$  (or  $n$ ),  $\bar{\rho}_{\text{bot}}/\bar{\rho}_{\text{top}}$ ,  $g_{\text{bot}}/(4\pi G \bar{\rho}_{\text{bot}} d)$ , and  $\gamma$ . For convenience, we replace the parameter  $\bar{\rho}_{\text{bot}}/\bar{\rho}_{\text{top}}$  with a radially averaged dissipation number  $\bar{Di} = \gamma \ln \bar{\rho}_{\text{bot}}/\bar{\rho}_{\text{top}}$ . In the Boussinesq limit,  $g_{\text{bot}}/(4\pi G \bar{\rho}_{\text{bot}} d)$  is the only parameter for the reference state.

## 3.2. The dynamic-state equations

Equations (2.7)–(2.10) are used to model compressible (anelastic) convection in which the reference-state quantities  $\bar{\rho}$  and  $\bar{T}$  are derived from the previous section. With this reference state, the dimensionless coefficients from (2.7)–(2.10) are

$$Di = -\frac{\gamma n d \Theta}{\Theta dr}, \quad (3.6)$$

$$Ra = -\gamma n \frac{\Delta T_{sa} (\bar{\rho}_{bot} c_p d)^2}{\eta k} \Theta^{2n-1} \frac{d\Theta}{dr}, \quad (3.7)$$

$$\frac{\bar{T}}{\Delta T_{sa}} = \frac{\bar{T}_{bot}}{\Delta T_{sa}} \Theta^{\gamma n}, \quad (3.8)$$

$$\alpha \bar{T} = \gamma \left( \frac{c_p \bar{T}_{bot}}{g_{bot} d} \right) \left( \frac{g_{bot}}{4\pi G \bar{\rho}_{bot} d} \right) \frac{d^2}{R^2} \Theta^{\gamma n-1}. \quad (3.9)$$

Therefore, the above relations introduce the three dimensionless numbers:  $\Delta T_{sa} (\bar{\rho}_{bot} c_p d)^2 / \eta k$  (equivalent to  $Ra/Di$  at the base of the shell),  $\bar{T}_{bot} / \Delta T_{sa}$  and  $c_p \bar{T}_{bot} / (g_{bot} d)$ . In the remainder of this paper we use a volume-averaged Rayleigh number  $\langle Ra \rangle$  rather than refer to  $(\Delta T_{sa} (\bar{\rho}_{bot} c_p d)^2 / (\eta k))$ . In summary, the non-dimensional input parameters to the numerical model are:

(i)  $K'$  (or  $n = 1/(K' - 1)$ ) which is held fixed at 3.5, characteristic of the Earth's whole mantle (Stacey 1977; Dzeiwonski & Anderson 1981);

(ii)  $\gamma = (\bar{\rho} / \bar{T}) (d\bar{T} / d\bar{\rho})$ , the Grüneisen parameter which is held fixed at 1, approximately true throughout the Earth's mantle;

(iii)  $\bar{Di} = \gamma \ln (\bar{\rho}_{bot} / \bar{\rho}_{top})$ , the radially averaged dissipation number which, in this study, is variable;

(iv)  $g_{bot} / (4\pi G \bar{\rho}_{bot} d)$  which is held fixed at 1.26;

(v)  $\bar{T}_{bot} / \Delta T_{sa}$  which, in this paper, is variable;

(vi)  $c_p \bar{T}_{bot} / (g_{bot} d)$  which is held constant at 0.12;

(vii)  $r_{bot} / r_{top}$  the inner to outer radius ratio, for this study, held fixed at 0.547, characteristic of the mantles of Earth, Mars and Venus.

(viii)  $\langle Ra \rangle$ , the volume-averaged Rayleigh number which is variable.

The continuity equation (2.1) is satisfied exactly by a poloidal mass flux:  $\bar{\rho} v = \nabla \times \nabla \times (W \hat{r})$ ; as in the infinite-Prandtl-number Boussinesq case, the toroidal flow is identically zero when the viscosity field is spherically symmetric (Chandrasekhar 1961; Glatzmaier 1988). Thus, the three dependent variables are  $W$ ,  $P'$  and  $S'$  and the three equations are  $\hat{r} \cdot (2.2)$ ,  $\nabla \cdot (2.2)$  and (2.3) (see Glatzmaier 1988). The boundaries of the shell are impermeable, shear-stress free and isothermal. Therefore, the boundary conditions at  $r_{top}$  and  $r_{bot}$  are

$$W = \frac{\partial^2 W}{\partial r^2} - \left( \frac{2}{r} - \frac{Di}{\gamma} \right) \frac{\partial W}{\partial r} = T' - T'_c = 0 \quad (3.10)$$

(Glatzmaier 1988). The superadiabatic part of the conductive temperature profile  $T'_c$  satisfies the equation

$$\nabla^2 (\bar{T} / \Delta T_{sa} + T'_c) = 0 \quad (3.11)$$

with isothermal boundary conditions

$$T'_c = \begin{cases} \beta & \text{at } r = r_{bot}; \\ \beta - 1 & \text{at } r_{top} \end{cases} \quad (3.12)$$

The parameter  $\beta$  (where  $0 \leq \beta \leq 1$ ) is adjusted to allow the convective temperature profile to coincide with the reference-state adiabat away from the thermal boundary layers.

### 3.3. The numerical method

Solutions to the equations of motion and energy are obtained through a spectral-transform Chebyshev-collocation method (Glatzmaier 1984, 1988). The dependent variables are expanded in terms of spherical harmonics and Chebyshev polynomials, for example,

$$W = \left(\frac{2}{N}\right)^{\frac{1}{2}} \sum_{l=0}^L \sum_{m=-l}^{+l} \sum_{n=0}^N W_{ln}^m (1 - \frac{1}{2}[\delta_{n0} + \delta_{nN}]) T_n(x) Y_l^m,$$

where

$$x = 2 \left( \frac{r - r_{\text{bot}}}{r_{\text{top}} - r_{\text{bot}}} \right) - 1, \quad T_n(x) = \cos(n \cos^{-1} x)$$

$$Y_l^m(\theta, \phi) = \left( \frac{2l+1}{4\pi} \frac{(l-m)!}{(l+m)!} \right)^{\frac{1}{2}} p_l^m(\cos \theta) e^{im\phi}.$$

The  $p_l^m$  are the associated Legendre polynomials of spherical harmonic degree  $l$  and order  $m$ , and the  $T_n$  are the Chebyshev polynomials of order  $n$ . The spectral expansions are only accurate if their power spectra near the truncation levels  $L$  and  $N$  have negligible power. Nonlinear terms are dealiased with an excessive grid point method. Time integration is performed via finite differences with a Crank–Nicolson scheme for the linear terms and an Adams–Bashforth method for the nonlinear terms. The time step size is constrained by the Courant condition. For more details on the numerical method, see Glatzmaier (1984, 1988).

### 3.4. Verification of the method

A verification of the model has been carried out in the Boussinesq limit (Bercovici *et al.* 1989c). However, this comparison could not validate parts of the model that are restricted to the anelastic formulation. We therefore carried out a linear stability analysis of compressible convection with both the numerical model described above and an independently developed Runge–Kutta, Newton–Raphson two-point boundary-value problem solver (see §4). The corroboration of results from the linear stability analysis extends the verification of the model to all the anelastic portions of the code save the viscous heating term (since it is non-linearizable). To complete the verification of the model, we have tested the calculation of viscous heating for an arbitrary poloidal velocity field against the same calculation made with a separate finite-difference numerical code. The poloidal velocity potential  $W$  used for the test is

$$W = \sum_{l=0}^L \sum_{m=0}^{+l} \sum_{n=1}^N \frac{l}{(l+1)^6} \frac{1}{n^2} \sqrt{2 \sin [n\pi(r-r_{\text{bot}})]} \left( \frac{2l+1}{(1+\delta_{m0}) 2\pi} \frac{(l-m)!}{(l+m)!} \right)^{\frac{1}{2}} P_l^m(\cos \theta) \cos(m\phi). \quad (3.13)$$

The calculation is made non-dimensional such that  $\eta = 1$ ,  $r_{\text{bot}} = 1.222$  and  $r_{\text{top}} = 2.222$ . For quantitative comparison, the viscous heating is transformed to  $(l, m, r)$ -space, and its volume integral for every  $l$  and  $m$  is calculated. These spectral components of viscous heating for the two codes are shown in table 1. The spectral components of the two codes agree within approximately 1% for the dominant values and within approximately 2% for the smaller terms. This test satisfactorily validates the calculation of viscous heating and completes the verification of the numerical model.

$l, m$	Model $\langle \Phi \rangle$	Test code $\langle \Phi \rangle$	Percent difference
0, 0	$1.82271 \times 10^{-1}$	$1.80688 \times 10^{-1}$	0.88
1, 0	$8.71182 \times 10^{-2}$	$8.62661 \times 10^{-2}$	0.99
1, 1	$5.66751 \times 10^{-2}$	$5.61256 \times 10^{-2}$	0.98
2, 0	$1.93986 \times 10^{-2}$	$1.91327 \times 10^{-2}$	1.39
2, 1	$-1.65630 \times 10^{-2}$	$-1.65988 \times 10^{-2}$	0.21
2, 2	$-3.16455 \times 10^{-3}$	$-3.23102 \times 10^{-3}$	2.06
3, 0	$6.46865 \times 10^{-3}$	$6.37402 \times 10^{-3}$	1.48
3, 1	$-1.10307 \times 10^{-2}$	$-1.10498 \times 10^{-2}$	0.17
3, 2	$-1.21119 \times 10^{-2}$	$-1.21100 \times 10^{-2}$	0.02
3, 3	$-6.17327 \times 10^{-3}$	$-6.18703 \times 10^{-3}$	0.22
4, 0	$2.02165 \times 10^{-3}$	$1.99338 \times 10^{-3}$	1.42
4, 1	$-4.52766 \times 10^{-3}$	$-4.56107 \times 10^{-3}$	0.73
4, 2	$-6.26190 \times 10^{-3}$	$-6.27876 \times 10^{-3}$	0.27
4, 3	$-6.12932 \times 10^{-3}$	$-6.13495 \times 10^{-3}$	0.09
4, 4	$-3.67061 \times 10^{-3}$	$-3.68791 \times 10^{-3}$	0.47
5, 0	$-8.20239 \times 10^{-4}$	$-8.28106 \times 10^{-4}$	0.95
5, 1	$-2.27443 \times 10^{-3}$	$-2.32422 \times 10^{-3}$	2.14
5, 2	$-3.22433 \times 10^{-3}$	$-3.25946 \times 10^{-3}$	1.08
5, 3	$-3.74585 \times 10^{-3}$	$-3.76782 \times 10^{-3}$	0.58
5, 4	$-3.63300 \times 10^{-3}$	$-3.65199 \times 10^{-3}$	0.52
5, 5	$-2.70319 \times 10^{-3}$	$-2.73021 \times 10^{-3}$	0.99

TABLE 1. Comparison of the volume integral of viscous heating  $\langle \Phi \rangle$  for every  $l$  and  $m$  for the spectral transform numerical model of this study (Model), and a finite-difference code (Test code) developed explicitly for calculating viscous heating. Equation (3.13) (with  $L = 5$  and  $N = 4$ ) for a poloidal velocity potential is used to generate the velocity field from which viscous heating is calculated. The spectral-transform code has 25 Chebyshev collocation points in radius, 20 Gauss-Legendre points in latitude, and 40 evenly spaced (Fourier) points in longitude. To compensate for the added accuracy of Chebyshev collocation and Gaussian quadrature, the finite-difference test code has a grid with 50, 41 and 81 evenly spaced radial, latitudinal and longitudinal grid points, respectively.

#### 4. Linear stability

The critical Rayleigh number  $\langle Ra \rangle_{cr}$  for the onset of convection is dependent on the spherical harmonic degree  $l$  and the non-dimensional parameters (i)–(vii) listed at the end of §3.2;  $\langle Ra \rangle$  is the eigenvalue of the linearized equations. In this paper we will only examine the dependence of  $\langle Ra \rangle_{cr}$  on  $\overline{D}i$ ,  $\overline{T}_{bot}/\Delta T_{sa}$ , and spherical harmonic degree.

As mentioned in §3.4, the linear stability analysis is carried out with two different techniques to check the numerical method. In one technique, the numerical model itself is used to time integrate the linearized conservation equations for various  $\langle Ra \rangle$ . For each spherical harmonic degree, the maximum real growth rate for the  $W_{ln}^m$  is monitored at each  $\langle Ra \rangle$ . The two Rayleigh numbers with small positive and negative real growth rates bracket  $\langle Ra \rangle_{cr}$ . Linear interpolation of the growth rate between these two values of  $\langle Ra \rangle$  is used to estimate  $\langle Ra \rangle_{cr}$ . The second method employs a Runge-Kutta, Newton-Raphson shooting scheme to solve the eigenvalue, two-point boundary-value problem posed by the linearized equations. The shooting scheme itself is verified by comparing its results in the plane-layer limit ( $r_{bot}/r_{top} \rightarrow 1$ ) to those of a previous analysis of plane-layer compressible convection (Jarvis & McKenzie 1980; see Bercovici 1989).

$\overline{Di}$	$\frac{\overline{T}_{\text{bot}}}{\Delta T_{\text{sa}}}$	$\langle Ra \rangle_{\text{cr}}$				
		$l = 1$	2	3	4	5
0		1919	915	<b>733</b>	751	878
0.25	1	2029	979	<b>795</b>	823	969
	10	1899	920	<b>750</b>	781	924
	30	1616	781	<b>633</b>	650	754
0.50	1	2140	1039	<b>847</b>	880	1037
	10	1481	722	<b>591</b>	616	727
	30	863	420	<b>342</b>	352	409

TABLE 2. Critical Rayleigh number  $\langle Ra \rangle_{\text{cr}}$  for the spherical shell anelastic model with  $r_{\text{bot}}/r_{\text{top}} = 0.547$  for different  $\overline{Di}$ ,  $\overline{T}_{\text{bot}}/\Delta T_{\text{sa}}$ , and  $l$ . The minimum  $\langle Ra \rangle_{\text{cr}}$  (shown in bold face) occurs at  $l = 3$  in all cases

Table 2 lists the  $\langle Ra \rangle_{\text{cr}}$  versus  $l$  for the parameters used in this paper. The  $\langle Ra \rangle_{\text{cr}}$  for  $\overline{T}_{\text{bot}}/\Delta T_{\text{sa}} = 1$  increases by only 16% from  $\overline{Di} = 0$  to 0.5; this is probably due to the slight stabilization of fluid near the top of the shell as  $\overline{Di}$  increases. At larger values of  $\overline{T}_{\text{bot}}/\Delta T_{\text{sa}}$ , increases in  $\overline{Di}$  have the opposite effect:  $\langle Ra \rangle_{\text{cr}}$  decreases (nearly 50% for  $\overline{T}_{\text{bot}}/\Delta T_{\text{sa}} = 30$ ) as  $\overline{Di}$  increases.

For large  $\overline{T}_{\text{bot}}/\Delta T_{\text{sa}}$ , the lower half of the shell is destabilized and the upper half is stabilized (figure 1). The stability of fluid near the top of the shell leads to a penetrative convection that is exactly opposite in nature to that of the plane-layer, constant- $Di$  case (Jarvis & McKenzie 1980). In the plane-layer model, the adiabatic temperature profile is an exponential function of height (which corresponds to  $K' = 1$  with gravity and  $\alpha$  constant) and the conductive temperature profile is linear. Therefore, the superadiabatic temperature gradient in the plane layer is positive in the lower half of the layer and negative in the upper half; and so, the top of the layer is unstable and the bottom is stable. This emphasizes the difference between spherical-shell and plane-layer convection, as well as the effect of the shape of the adiabat, which is controlled by  $K'$  (or  $n$ ). Penetrative flow at the base of the fluid layer was also found in the compressible spherical-shell study of Machetel & Yuen (1989). This occurred because that study varied the amount of internal heating until the basal heat flux was very low, leading to a subadiabatic temperature gradient near the base of the shell. That study also used a constant  $Di$ , leading to a very steep adiabat near the base of the shell which influenced the internal heating rate at which penetrative flow occurred.

Since the critical Rayleigh number is strongly dependent on other parameters, it is impossible to hold both the relative convective vigour (measured by  $\langle Ra \rangle / \langle Ra \rangle_{\text{cr}}$ ) and the magnitude of flow-induced heating (measured by  $\overline{Di} / \langle Ra \rangle$ ) fixed while exploring the effects of other parameters. Therefore, in §5, we examine the effects of various parameters on nonlinear convection while holding  $\langle Ra \rangle$  constant at 8000, except for  $\overline{Di} = 0.5$  and  $\overline{T}_{\text{bot}}/\Delta T_{\text{sa}} = 30$ , when we use  $\langle Ra \rangle = 4000$ . Therefore,  $\langle Ra \rangle$  is maintained at approximately  $10 \langle Ra \rangle_{\text{cr}}$  while effecting as little change as possible on  $\overline{Di} / \langle Ra \rangle$  (for a given  $\langle Ra \rangle$ ).

## 5. Nonlinear solutions for $\langle Ra \rangle \approx 10 \langle Ra \rangle_{\text{cr}}$

In this section, we examine the effects of varying  $\overline{Di}$  and  $\overline{T}_{\text{bot}}/\Delta T_{\text{sa}}$  at relatively low  $\langle Ra \rangle$  ( $\langle Ra \rangle \approx 10 \langle Ra \rangle_{\text{cr}}$ ). Using a steady Boussinesq solution from Bercovici *et al.*

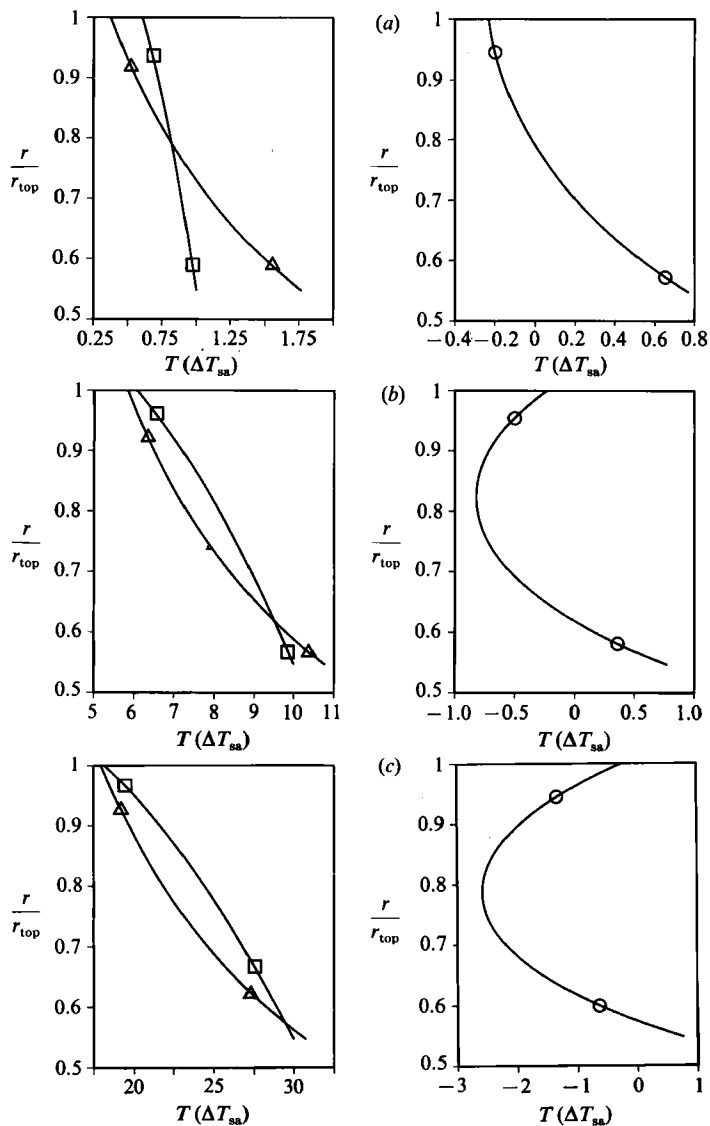


FIGURE 1. Adiabatic ( $\square$ ) and conductive ( $\triangle$ ) temperature profiles (left panels) and superadiabatic ( $\circ$ ) temperature profiles in units of  $\Delta T_{sa}$  for  $\overline{Di} = 0.5$ : (a)  $T_{bot}/\Delta T_{sa} = 1$ ; (b) 10; (c) 30.

(1989c) as an initial condition, we obtain a steady solution for the case  $\langle Ra \rangle = 8000$ ,  $\overline{Di} = 0$ ,  $\overline{T}_{bot}/\Delta T_{sa} = 1$ . This solution has a convective pattern with tetrahedral symmetry (i.e. dominated by the  $l = 3$ ,  $m = 2$  spherical harmonic mode). This solution is then used to obtain solutions for the cases  $\langle Ra \rangle = 8000$ ,  $\overline{Di} = 0.25$ ,  $\overline{T}_{bot}/\Delta T_{sa} = 1, 10$  and  $30$ ;  $\langle Ra \rangle = 8000$ ,  $\overline{Di} = 0.5$ ,  $\overline{T}_{bot}/\Delta T_{sa} = 1$  and  $10$ ;  $\langle Ra \rangle = 4000$  (to keep  $\langle Ra \rangle$  near to  $10\langle Ra \rangle_{cr}$ ),  $\overline{Di} = 0.5$ ,  $\overline{T}_{bot}/\Delta T_{sa} = 30$ . In those cases when  $\overline{T}_{bot}/\Delta T_{sa} = 1$  truncation levels of  $L = 21$ ,  $N = 16$  are used, while for  $\overline{T}_{bot}/\Delta T_{sa} = 10$  and  $30$ ,  $L = 31$  is used, the reasons for which will become apparent shortly. Figure 2 shows power spectra for volume-averaged entropy variance and kinetic energy in both the spherical harmonic and Chebyshev spectral domains for the different

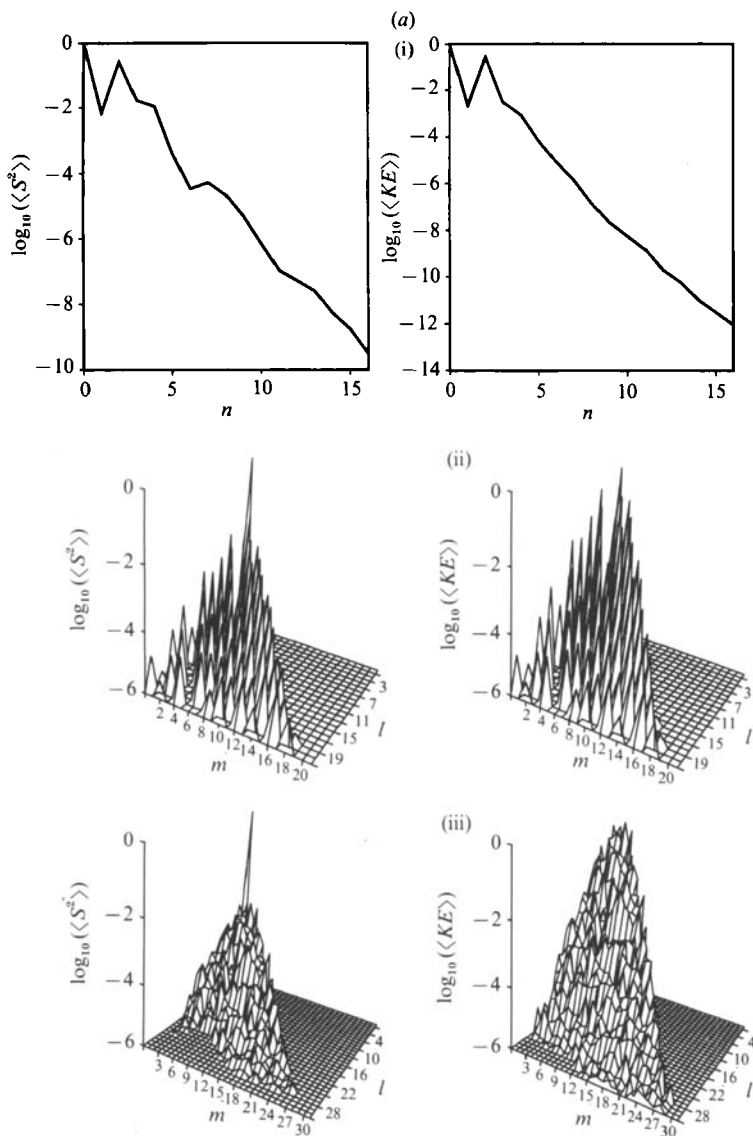


FIGURE 2(a). For caption see facing page.

truncation levels. A net drop of four orders of magnitude or more in power indicates that a solution is well resolved (see the Appendix for a convergence test). That the kinetic energy is better resolved than the entropy variance is typical of high-Prandtl-number flow.

### 5.1. Temperature and entropy profiles

Figure 3 shows spherically averaged temperature and entropy profiles for the nonlinear solutions with different  $\overline{Di}$  and  $\overline{T}_{\text{bot}}/\Delta T_{\text{sa}}$ . The central portion of the shell (i.e. away from the thermal boundary layers) is subadiabatic for all  $\overline{Di}$ . When the superadiabatic temperature drop  $\Delta T_{\text{sa}}$  is large ( $\overline{T}_{\text{bot}}/\Delta T_{\text{sa}} = 1$ ), the thermal boundary layers are fully destabilized for all  $\overline{Di}$ . As  $\Delta T_{\text{sa}}$  decreases for  $\overline{Di} > 0$  the total temperature gradient near the top of the shell (where the heat flow per unit area is

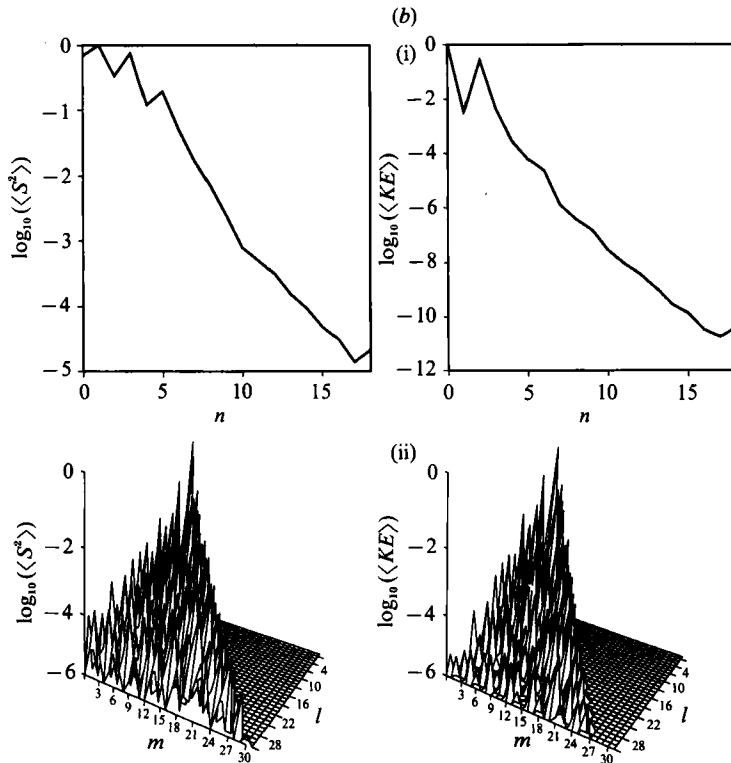


FIGURE 2. Characteristic power spectra of (i) Chebyshev and (ii), (iii) spherical harmonic expansions for entropy variance (left panels) and kinetic energy (right panels) for cases with (a)  $\langle Ra \rangle \approx 10 \langle Ra \rangle_{cr}$  (the second set of spherical harmonic spectra (iii) are for the time-dependent cases with  $\bar{T}_{bot}/\Delta T_{sa} = 30$  in which  $L = 31$ ); and (b)  $\langle Ra \rangle \approx 100 \langle Ra \rangle_{cr}$ .

smallest) becomes smaller in magnitude than the adiabatic temperature gradient. Thus, at the top of the shell, the fluid is subadiabatic and stable; this is the exact opposite of the plane-layer, constant- $\overline{Di}$  case (Jarvis & McKenzie 1980) and the internally heated spherical-shell case (Machetel & Yuen 1989) (see discussion in §4).

### 5.2. Patterns of convection and the horizontal structure of the velocity and thermal fields

The convective pattern for  $\bar{T}_{bot}/\Delta T_{sa} = 1$  and all  $\overline{Di}$  has a dominant tetrahedral ( $l = 3, m = 2$ ) signature. As in the Boussinesq case of Bercovici *et al.* (1989c), the upwellings are in the form of cylindrical plumes surrounded by an interconnected network of downwelling sheets (figure 4). The entropy contours display sharper upwelling and downwelling features than the radial velocity contours because of the infinite  $Pr$ . The maximum upwelling and downwelling velocities and entropy anomalies increase slightly with  $\overline{Di}$ . The change in velocities probably occurs because the mass flux is essentially the same for the different  $\overline{Di}$  and since the density decreases with height for non-zero  $\overline{Di}$ , the vertical velocities increase accordingly.

As shown in §5.1, when  $\bar{T}_{bot}/\Delta T_{sa}$  increases for  $\overline{Di} > 0$ , the entropy drop across the upper thermal boundary layer decreases and even reverses its sign. This leads to a weakening and eventually a complete loss of fine downwelling structure. For both  $\overline{Di} = 0.25$  and  $0.5$ , the tetrahedral pattern remains as  $\bar{T}_{bot}/\Delta T_{sa}$  increases from 1 to 10.

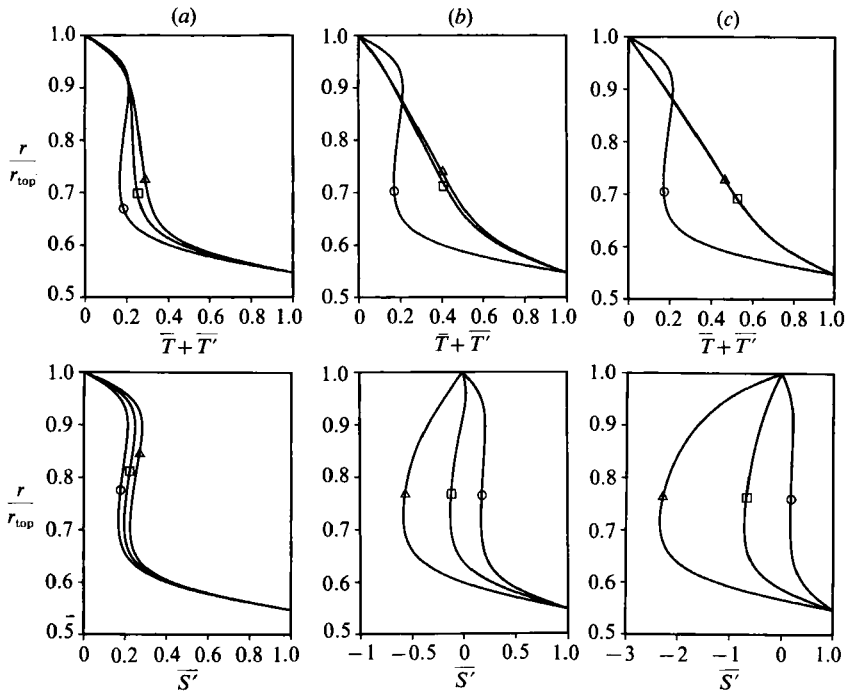


FIGURE 3. Radial profiles of spherically averaged temperature (top panels) and entropy (bottom panels) for  $\bar{D}i = 0$  ( $\circ$ ),  $0.25$  ( $\square$ ) and  $0.5$  ( $\triangle$ ) with  $\langle Ra \rangle \approx 10 \langle Ra \rangle_{cr}$ . (a)  $\bar{T}_{bot}/\Delta T_{sa} = 1$ ; (b) 10; (c) 30.

(The dependence on  $\bar{T}_{bot}/\Delta T_{sa}$  for the case with  $\bar{D}i = 0.25$  is essentially identical to that with  $\bar{D}i = 0.5$  and is therefore not shown.) Nevertheless, the downwelling regions become less concentrated. As  $\bar{T}_{bot}/\Delta T_{sa}$  further increases to 30, the pattern loses all polyhedral symmetry; the downwelling structure is virtually nonexistent while the upwelling is contained in many (on the order of 10) narrow, concentrated cylindrical plumes. (The transition to this pattern with small-wavelength features was the reason for the increase in  $L$  from 21 to 31.) This is the opposite of what occurred in the plane layer, constant- $Di$  study (Jarvis & McKenzie 1980) and the internally heated spherical shell study (Machetel & Yuen 1989) wherein the upwellings were virtually eliminated and the downwellings became highly narrow and concentrated. Therefore, in those studies, the broadening of upwellings and narrowing of downwellings was due to the elimination of the lower boundary layer and enhancement of the upper one, and not (as suggested by Jarvis & McKenzie 1980) from the decompression (compression) of upwelling (downwelling) currents.

As  $\bar{T}_{bot}/\Delta T_{sa}$  increases, the unstable portion of the fluid is confined to an ever thinner layer in the lower portion of the shell. This causes the horizontal scale of the convection cells to decrease as  $\bar{T}_{bot}/\Delta T_{sa}$  increases, leading to more upwelling plumes. For both  $\bar{D}i = 0.25$  and  $0.5$ , the solutions at  $\bar{T}_{bot}/\Delta T_{sa} = 30$  are time dependent; this will be discussed further in §5.5.

The radial velocity and entropy extrema in table 3 show that the upwelling regions become relatively hotter and faster and downwelling regions become warmer and slower as the superadiabatic temperature drop  $\Delta T_{sa}$  decreases. The downwellings lose vigour as  $\bar{T}_{bot}/\Delta T_{sa}$  increases because the upper boundary layer becomes stabilized. The vigour of upwelling increases because the relative entropy drop across the lower

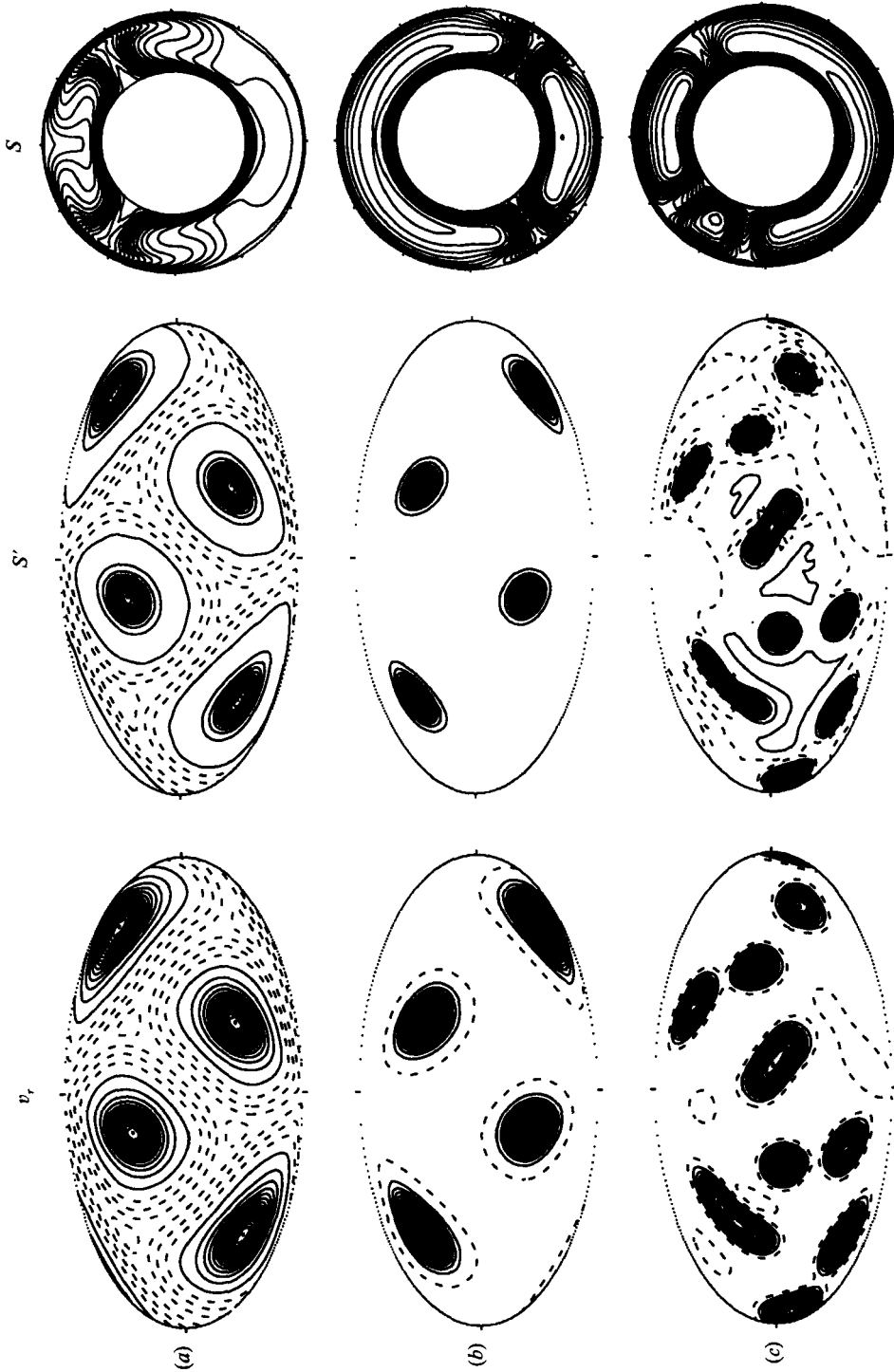


FIGURE 4. Contours of radial velocity  $v_r$  and entropy anomalies  $S'$  (i.e. entropy with respect to the spherically symmetric state) at a surface of constant radius  $r/r_{\text{top}} = 0.77$  (i.e. at mid-depth), and contours of total entropy  $S$  in a meridional cross-section for  $Di = 0.5$  and  $\langle Ra \rangle \approx 10 \langle Ra \rangle_{cr}$ . See table 3 for contouring information. For contours on the constant-radius surface, solid contours denote positive values and dashed contours denote negative values. (a)  $T_{\text{bot}}/\Delta T_{\text{sa}} = 1$ ; (b) 10; (c) 30.

$\frac{\bar{T}_{bot}}{\Delta T_{sa}}$	$v_r$			$S'$			$S$		
	1	10	30	1	10	30	1	10	30
$f_{min}$	-40	-10	-18	-0.18	0	-0.20	-0.35	-1.0	-2.6
$f_{max}$	150	230	130	0.84	1.50	2.3	0.77	0.80	0.80
$\Delta f$	10	10	9	0.06	0.10	0.10	0.07	0.10	0.20

TABLE 3. Contour information for figure 4, where  $f_{min}$  is the minimum contour value,  $f_{max}$  is the maximum contour value, and  $\Delta f$  is the contour interval for the variable presented in the top row

boundary layer increases to compensate for the entropy rise in the upper half of the shell.

### 5.3. Vertical structure

The vertical structure of the entropy field is not affected significantly by changes in dissipation number when  $\bar{T}_{bot}/\Delta T_{sa} = 1$ . The upwelling plumes have fairly broad necks and well-defined mushroom heads as the plumes push into the upper boundary layer (figure 4). The upwelling plumes in most of the cases shown are typically thicker than the horizontal boundary layers. This is not an artifact of the numerical resolution but results from the fluid in the plume moving along a line in the meridional plane of the figure while most of the fluid in the horizontal boundary layer is out of the meridional plane (see the Appendix). Figure 4 also shows that the downwelling regions are not as concentrated as the upwelling regions. As  $\bar{T}_{bot}/\Delta T_{sa}$  increases to 10, the upwellings narrow and the downwellings broaden. For  $\bar{T}_{bot}/\Delta T_{sa} = 30$ , the upwelling plumes are very narrow and do not form mushroom heads at the top boundary since they penetrate into the stable upper portion of the shell. Although the fluid in the upper half of the shell outside of the plumes is largely stable and conductive, it subsides with a small downward velocity to compensate for the upward mass flux of the plumes; this fluid thus comprises the broad weak downwelling.

### 5.4 Heat generation and transport

A global measure of the efficiency of heat transport by convection is the Nusselt number  $Nu$  (the ratio of spherically averaged total heat flow to heat flow in the purely conductive state). By conservation of energy, in a steady state  $Nu$  should be the same at the top and bottom of the shell; the percent difference between these  $Nu$  is a global measure of the accuracy of the solutions and in this paper is never more than 1.5%. For cases with  $\langle Ra \rangle \approx 10 \langle Ra \rangle_{cr}$ ,  $Nu$  decreases with increasing  $\bar{D}i$  or  $\bar{T}_{bot}/\Delta T_{sa}$ . For  $\bar{D}i = 0$ ,  $Nu$  is 3.62. When  $\bar{T}_{bot}/\Delta T_{sa} = 1$ ,  $Nu$  is 3.21 and 3.01 for  $\bar{D}i = 0.25$  and 0.5, respectively; when  $\bar{T}_{bot}/\Delta T_{sa} = 10$ ,  $Nu = 1.77$  and 1.65 for  $\bar{D}i = 0.25$  and 0.5. When  $\bar{T}_{bot}/\Delta T_{sa}$  equals 30, the solutions are time dependent, and  $Nu$  varies between 1.41 and 1.44 for both  $\bar{D}i = 0.25$  and 0.5. For a given  $\langle Ra \rangle$ , the Nusselt number decreases with  $\bar{D}i$  and  $\bar{T}_{bot}/\Delta T_{sa}$  because

$$Nu = 1 - \left[ \frac{(d/dr) (\bar{T}' - T'_c)}{\left(1 + \frac{\bar{T}_{bot} - \bar{T}_{top}}{\Delta T_{sa}}\right) \frac{r_{top} r_{bot}}{r^2}} \right]_{r=r_{top}, r_{bot}} \tag{5.1}$$

(where  $\bar{T}_{top} = \bar{T}_{bot} e^{-\bar{D}i}$ ) and if either  $\bar{D}i$  or  $\bar{T}_{bot}/\Delta T_{sa}$  increases,  $(\bar{T}_{bot} - \bar{T}_{top})/\Delta T_{sa}$  increases while  $\bar{T}'$  and  $T'_c$  are of order unity.

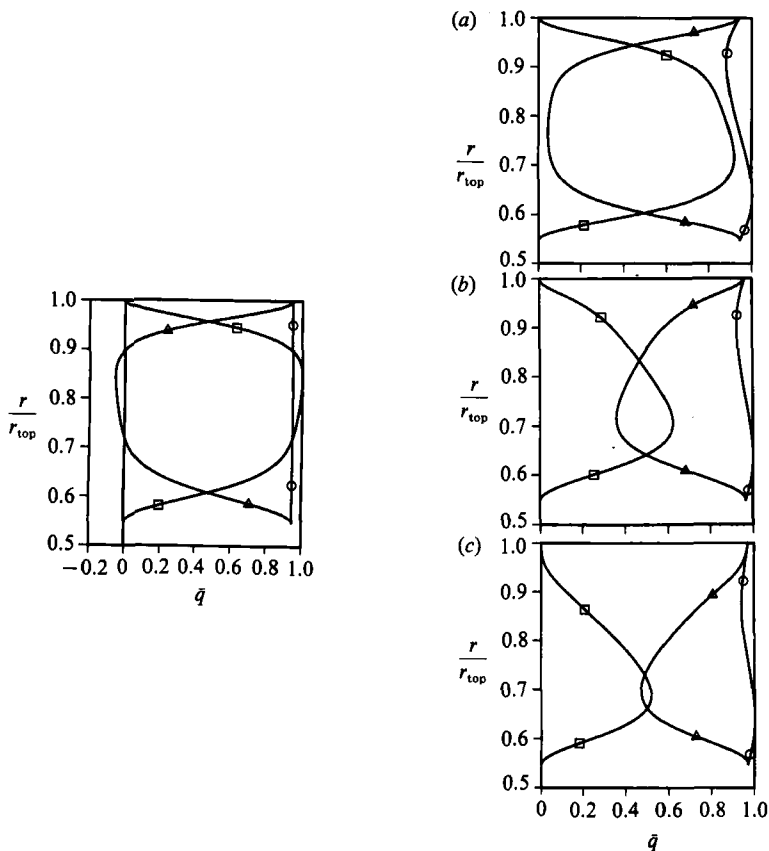


FIGURE 5. Radial profiles of surface-integrated conductive ( $\Delta$ ), advective ( $\square$ ) and total ( $\circ$ ) heat flow for  $\overline{Di} = 0$  (left) and 0.5 (right) with (a)  $\overline{T}_{\text{bot}}/\Delta T_{\text{sa}} = 1$ ; (b) 10; (c) 30. Values are normalized by the maximum heat flow.

The total advective and conductive heat fluxes across any spherical surface  $A$  are

$$\overline{q}_a = \frac{\overline{T}\overline{\rho}}{\overline{T}_{\text{bot}}\overline{\rho}_{\text{bot}}} \int_A v_r S' dA \tag{5.2}$$

and

$$\overline{q}_c = - \int_A \frac{\partial}{\partial r} \left( \frac{\overline{T}}{\Delta T_{\text{sa}}} + T^v \right) dA, \tag{5.3}$$

respectively. These two quantities and their sum are shown in figure 5. Conduction is the dominant form of heat transport in the boundary layers while advection dominates in the shell's interior. For  $\overline{Di} = 0$ , a small negative conductive heat flow occurs in the shell's interior because of the slightly subadiabatic temperature gradient there. The total heat flux is constant throughout the shell because there are no heat sources within the shell when  $\overline{Di} = 0$ . For  $\overline{Di} > 0$  (only  $\overline{Di} = 0.5$  is shown), the conductive heat flux is positive everywhere because the adiabat contributes a positive conductive heat flow. As  $\overline{T}_{\text{bot}}/\Delta T_{\text{sa}}$  increases, conduction assumes a larger role in the net heat transport because the adiabat carries a greater portion of the heat

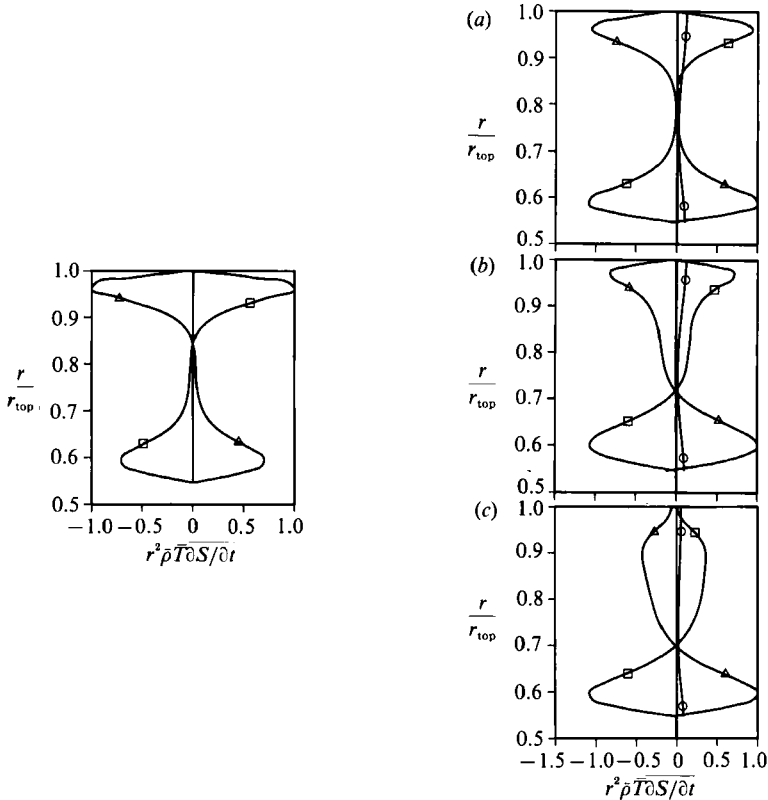


FIGURE 6. Radial profiles of surface-integrated advective ( $\square$ ), diffusive ( $\triangle$ ) and viscous ( $\circ$ ) heating terms for the same cases as in figure 5. Values are normalized by the maximum heating.

flow while the thermal anomalies (which scale as  $\Delta T_{sa}$ ) transported by advection become relatively smaller. The advective heat flow maximum and the conductive heat flow minimum move to greater depths as  $\bar{T}_{bot}/\Delta T_{sa}$  increases because the upper portion of the shell becomes more stabilized. The total heat flow for  $\bar{Di} > 0$  is not constant throughout the shell because heat sources and sinks are present in the forms of viscous and adiabatic heating.

Radial profiles of the surface-integrated terms in the energy equation (2.9) that contribute to the net heating of the shell  $\bar{\rho}\bar{T}\partial S'/\partial t$  are shown in figure 6. (The negative of the advection term is shown since it indicates advective heating.) The diffusion term is large and positive (negative) near the shell's base (top) where the boundary layer is conductively heated (cooled) from below (above). Advection is also large in the boundary layers as it cools (heats) the lower (upper) boundary layer. At  $\bar{Di} = 0$ , the advection and diffusion curves are symmetric about the zero heating line, which is expected since their sum must equal zero in steady state. In this case, advection and diffusion heat and cool the upper boundary layer more than they cool and heat the lower boundary layer which probably reflects the different curvatures of the top and bottom boundaries.

For  $\bar{Di} > 0$ , viscous heating is significant (i.e. between 1% and 10% of the other heating terms); it is largest in the boundary layers and smallest in the middle of the shell. Because viscous heating is always positive, the advection and diffusion terms are no longer equal in magnitude at any given radius. As  $\bar{Di}$  and  $\bar{T}_{bot}/\Delta T_{sa}$  increase,

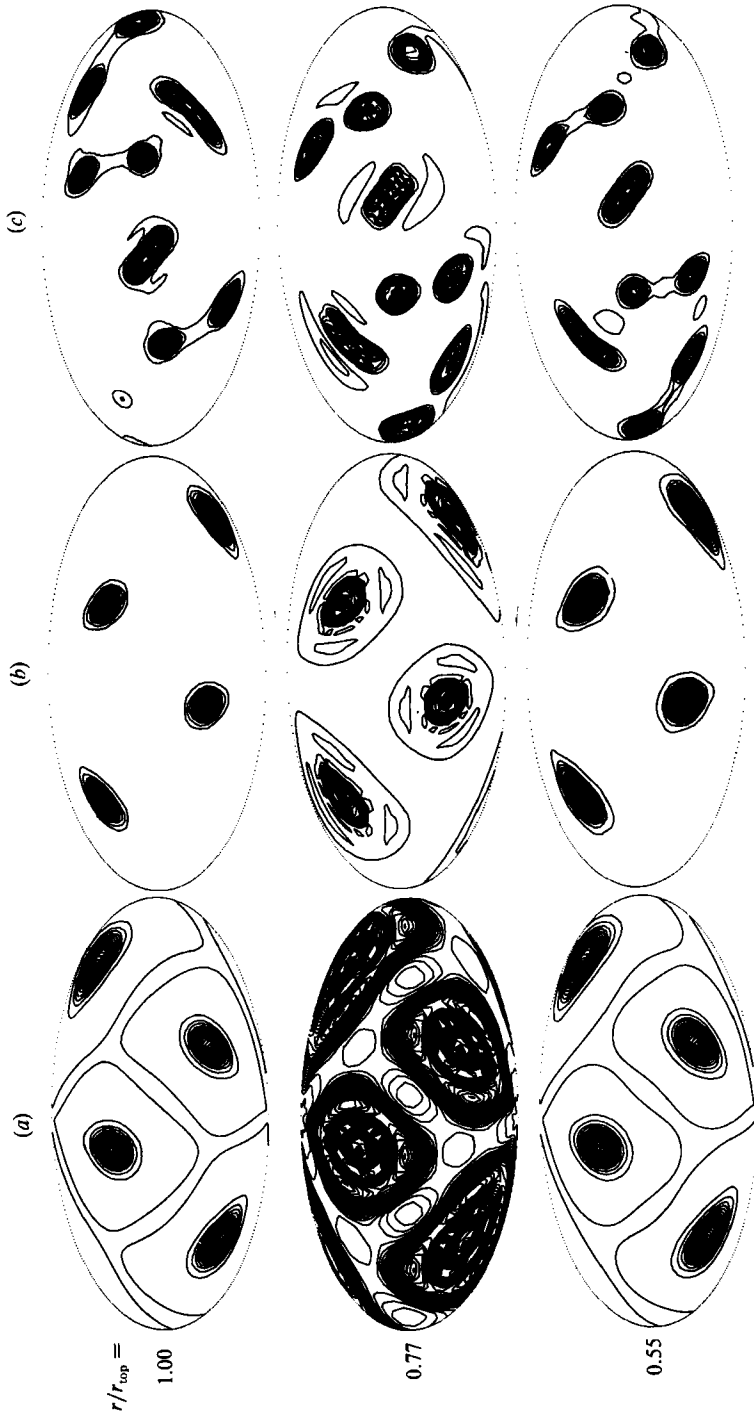


FIGURE 7. Contours of viscous heating at different depths for  $\bar{Di} = 0.5$  with (a)  $T_{\text{bot}}/\Delta T_{\text{ss}} = 1$ ; (b) 10; (c) 30. Viscous heating is non-dimensionalized by  $k\Delta T_{\text{ss}}/d^2$ . See table 4 for contouring information.

$\frac{T_{\text{bot}}}{\Delta T_{\text{sa}}}$	1	1	1	10	10	10	30	30	30
$\frac{r}{r_{\text{top}}}$	1	0.77	0.55	1	0.77	0.55	1	0.77	0.55
$\Phi_{\text{max}}$	21.250	1.208	49.989	49.989	5.416	112.476	32.493	11.997	119.970
$\Delta\Phi$	1.250	0.042	2.941	2.941	0.333	4.166	1.250	0.750	7.498

TABLE 4. Contour information for the viscous heating contours of figure 7, where  $\Phi_{\text{max}}$  is the maximum contour value, and  $\Delta\Phi$  is the contour interval;  $\Phi_{\text{min}}$ , the minimum contour value, is always 0. Viscous heating is non-dimensionalized by  $k\Delta T_{\text{sa}}/d^2$ .

the upper portion of the shell becomes increasingly stabilized causing advection to deposit more heat in the shell's interior and less in the upper boundary layer.

Figure 7 shows the spatial distribution of viscous heating. Viscous heating at mid-depth is highly concentrated in and around the upwelling plumes. When  $\overline{Di} > 0$  and  $\overline{T}_{\text{bot}}/\Delta T_{\text{sa}} = 1$ , the viscous heating associated with each plume is contained within three bands centred on the plume's axis. The outermost band surrounding the plume is in the downwelling shear zone adjacent to the plume. The other bands inside the upwelling region are probably due to the non-uniform thermal buoyancy of the plume which is highly focused at the plume centre (see figure 4). At the top and bottom of the shell, viscous heating is concentrated directly above or below the upwelling and downwelling regions. The point of maximum viscous heating in the shell occurs where the upwelling plumes meet the upper or lower boundary. This corresponds to the observation by Jarvis & McKenzie (1980) that viscous heating is greatest at the corners of a two-dimensional convection cell.

### 5.5. Time dependence

As noted in §5.2, when  $\overline{T}_{\text{bot}}/\Delta T_{\text{sa}} = 30$  for  $\overline{Di} > 0$ , the polyhedral symmetry of the convective pattern is broken and the solutions are time dependent at  $\langle Ra \rangle \approx 10\langle Ra \rangle_{\text{cr}}$ . In these cases, the convective pattern is characterized at any one time by roughly ten narrow cylindrical plumes (figure 8). Though these plumes fuse with one another, the total number of plumes remains about the same since plumes continuously form.

When  $\overline{Di} = 0.5$  and  $\overline{T}_{\text{bot}}/\Delta T_{\text{sa}} = 30$ , a convective pattern with a single dominant mode at  $l = 6$ ,  $m = 4$  is stable for a very long time (figure 8a). This pattern has fourteen plumes and therefore does not have the regular polyhedral symmetry. After approximately 0.4 diffusion timescales  $\tau_{\text{diff}} = d^2\bar{\rho}_{\text{bot}}c_p/k$  or roughly 14 overturn times, the pattern breaks down. The cluster of five plumes in the left hemisphere rapidly collapses to one plume (by time  $t = 1.118$ ) at the equator. The fusion of these plumes correlates with an increase in the maximum velocity (table 5). This probably results from the entire upwelling region being squeezed into a smaller horizontal area and/or the net viscous shear resistance to the upwelling being reduced (since the regions of shear between plumes are eliminated at the same time that the net surface area of the upwellings diminishes). Once the pattern becomes a random distribution of plumes, its evolution is characterized by a continuous formation and fusion of plumes.

Figure 8(b) shows time series and corresponding frequency-power spectra for the volume-integrated kinetic energy  $\langle KE \rangle$  of the above solutions. In the same way that

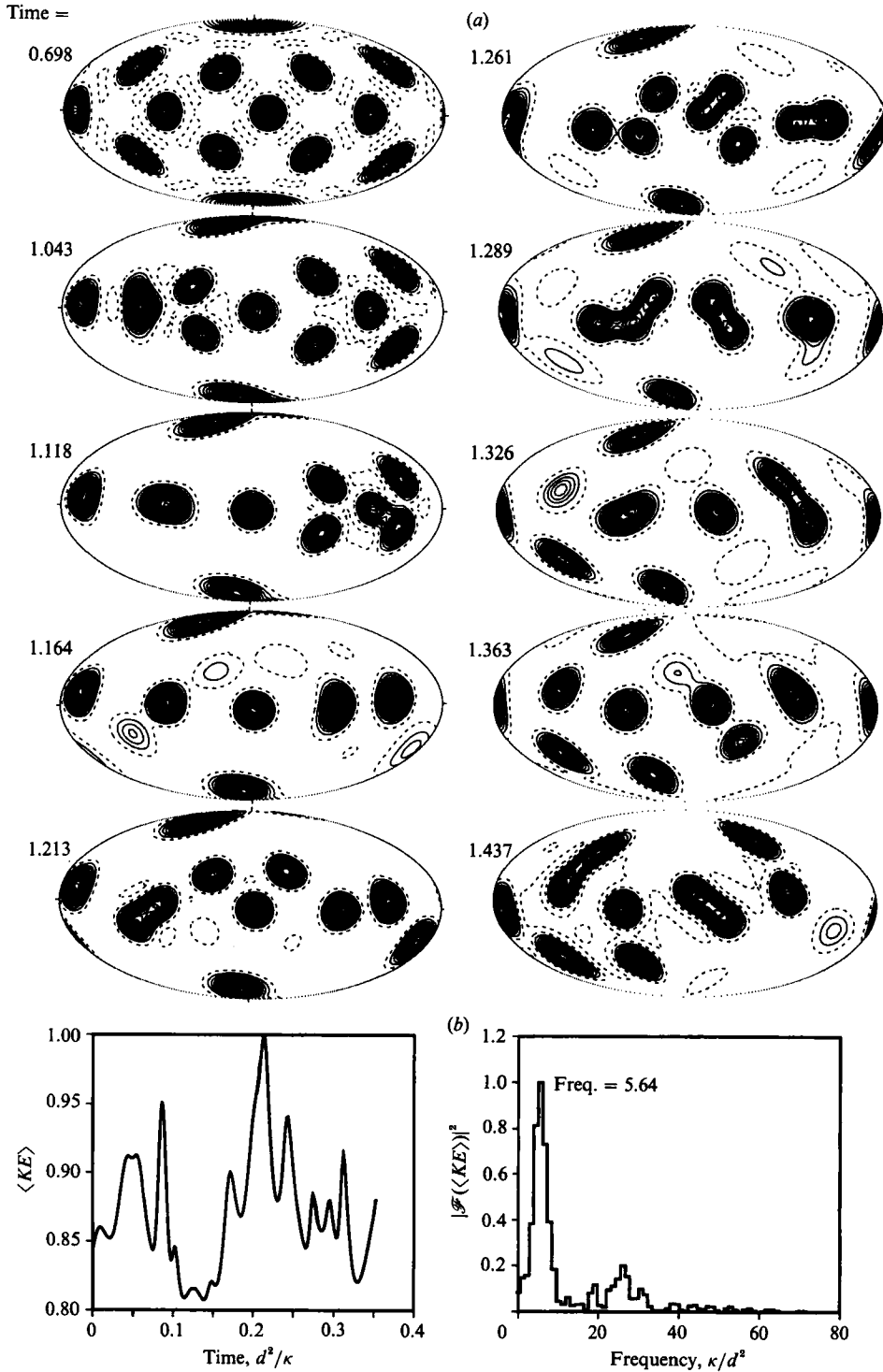


FIGURE 8. (a) Contours of radial velocity at different non-dimensional times for  $\overline{Di} = 0.5$  and  $\overline{T}_{bot}/\Delta T_{ss} = 30$ ; solid contours denote positive radial velocity and dashed contours denote negative radial velocity. (b) Volume-averaged kinetic energy  $\langle KE \rangle$  as a function of time and the corresponding Fourier power spectrum. See table 5 for contouring information regarding (a).

Time	0.698	1.043	1.118	1.164	1.213	1.437
$v_{r\min}$	-17.31	-17.31	-17.31	-8.66	-17.31	-17.31
$v_{r\max}$	121.17	147.14	155.79	164.45	147.14	129.83
$\Delta v_r$	8.66	8.66	8.66	8.66	8.66	8.66

TABLE 5. Contour information for the radial velocity contours of figure 8(a), where  $v_{r\min}$  is the minimum contour value,  $v_{r\max}$  is the maximum contour value, and  $\Delta v_r$  is the contour interval. Contour information for the first and last times are listed and information for any intermediate time is only shown when it is different from the previous time.

radial velocity increases with plume fusion, the large jumps in  $\langle KE \rangle$  signal the fusion of plumes. The dominant non-dimensional frequency for the  $\overline{Di} = 0.5$  case is at 5.6, characteristic of the envelope of the peaks in  $\langle KE \rangle$ . A secondary peak occurs at a frequency of 26.0 with roughly 20% of the power at the largest frequency; this frequency is characteristic of the period between peaks in  $\langle KE \rangle$ . These frequencies are considerably less than the overturn frequency (based on the maximum upwelling velocity in table 5); plume fusion occurs only once every four or five overturns.

## 6. Nonlinear solutions: $\langle Ra \rangle > 100\langle Ra \rangle_{cr}$

### 6.1. Solutions for $10\langle Ra \rangle_{cr} \leq \langle Ra \rangle \leq 100\langle Ra \rangle_{cr}$ and $\overline{T}_{bot}/\Delta T_{sa} = 1$

The solutions from §5 for  $\overline{Di} \geq 0$  and  $\overline{T}_{bot}/\Delta T_{sa} = 1$  were stepped up in Rayleigh number to  $\langle Ra \rangle = 80000$ ; all of these solutions were found to be steady. Compressibility has very little influence on the three-dimensional structure of solutions with  $\overline{T}_{bot}/\Delta T_{sa} = 1$ . The patterns of convection are identical and quantitative changes (e.g. the maximum velocity) are only on the order of 10% and not significantly different from what was discussed in §5. These solutions are similar to those for the Boussinesq case, hence we defer to Bercovici *et al.* (1989c) for a discussion of Boussinesq three-dimensional convection with increasing Rayleigh number. For further discussion of the compressible solutions, see Bercovici (1989).

Compressibility does have a small effect on the Nusselt number–Rayleigh number relationship. Figure 9 shows Nusselt versus Rayleigh numbers for  $\overline{Di} = 0, 0.25$  and  $0.5$ . As discussed in §5.4,  $Nu$  decreases with increasing  $\overline{Di}$ . If  $Nu \sim \langle Ra \rangle^\mu$ , then a least-squares fit to the  $Nu$  vs.  $\langle Ra \rangle$  curves gives  $\mu \approx 0.26$  for all three  $\overline{Di}$ . When points for  $\langle Ra \rangle < 40000$  are included,  $\mu$  decreases slightly (on the order of 2 or 3%) as  $\overline{Di}$  increases from 0 to 0.5. Thus, when  $\overline{T}_{bot}/\Delta T_{sa} = 1$ , changes in  $\overline{Di}$  do not appear to significantly affect the exponent of the  $Nu$ – $Ra$  relationship. Surface-integrated heat flow and volumetric heating do not change significantly with  $\langle Ra \rangle$  and vary with  $\overline{Di}$  similarly to what is discussed in §5.

### 6.2. Time dependence for the Case $\langle Ra \rangle = 16000$ , $\overline{Di} = 0.5$ , $\overline{T}_{bot}/\Delta T_{sa} = 10$

When  $\langle Ra \rangle$  for the solution with  $\overline{Di} = 0.5$  and  $\overline{T}_{bot}/\Delta T_{sa} = 10$  is increased from 8000 to 16000, the steady tetrahedral pattern disappears and is replaced by a pattern with a dominant spherical harmonic mode at  $l = 6$ ,  $m = 4$  (figure 10a), similar to the case with  $\langle Ra \rangle = 4000$ ,  $\overline{Di} = 0.5$ ,  $\overline{T}_{bot}/\Delta T_{sa} = 30$ . This pattern is probably established because it has a high-wavenumber mode (which is preferred when the unstable portion of the shell is effectively thinned as convection becomes penetrative) that has immediate access to the energy in the tetrahedral mode (via the quadratic nonlinear

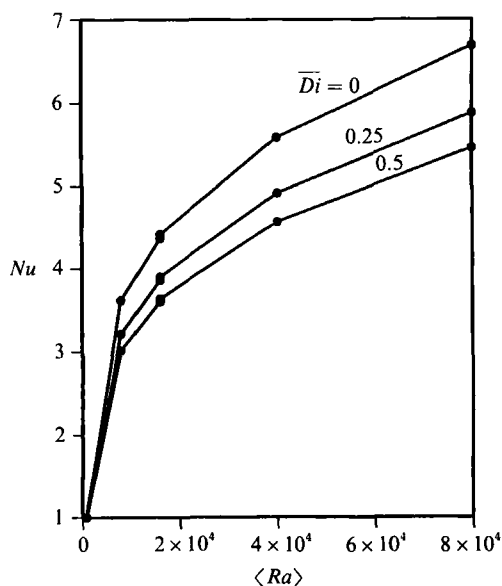


FIGURE 9. Nusselt number  $Nu$  versus Rayleigh number  $\langle Ra \rangle$  for three different  $\overline{Di}$ .

interaction of thermal advection). The  $l = 6$ ,  $m = 4$  pattern persists and is nearly steady for a very long time ( $0.7\tau_{\text{diff}}$ , or approximately 10000 time steps) after which the solution rapidly evolves to one with a dominant cubic ( $l = 4$ ,  $m = 0$  and  $l = 4$ ,  $m = 4$ ) signature. (The kinetic energy time series shown in figure 10*b* begins once the  $l = 6$ ,  $m = 4$  solution becomes unsteady.) The transition to the cubic pattern is evident in the  $\langle KE \rangle$  time series as the two sharp peaks in kinetic energy at  $t \approx 0.1$ . Except for a brief distortion of the polar plumes at  $t \approx 0.26$ , the cubic solution persists until  $t \approx 0.4$ . After this, the cubic pattern becomes unstable and eventually evolves into an irregular pattern with four plumes. The four-plume pattern itself becomes unstable after some time as the four plumes collapse to two plumes. Eventually, the two plumes become connected by sheets of upwelling to form a contiguous ring of upwelling by  $t \approx 1.4$ . An upwelling plume then forms at the centre of the ring by  $t \approx 1.6$  and the ring collapses to a plume antipodal to the newly formed plume ( $t \approx 1.8$ ). This is followed by an apparent repetition of the process by which two plumes are connected by a contiguous ring of upwelling ( $t \approx 2.4$ ); however, this ring is more or less orthogonal to the ring at  $t \approx 1.4$ . In between many of the time frames shown, the simulation displays very erratic behaviour in which plumes form and lose appendages, new plumes appear and vanish, etc. The time dependence of the kinetic energy of this case (figure 10*b*) is highly irregular and is generally sporadic, showing the most oscillations during the flurries of activity in the convective pattern.

The Nusselt number at the top of the shell for this case varies slightly from 1.78 to 1.82, while at the bottom of the shell  $Nu$  varies between 1.72 and 1.92. The greater variability in  $Nu$  at the base of the shell probably reflects the time-dependent behaviour of the plumes occurring through instabilities in the bottom boundary layer.

### 6.3. Time dependence for irregular convective patterns

Although the regular polyhedral patterns are steady at least up to  $\langle Ra \rangle \approx 100\langle Ra \rangle_{\text{cr}}$  (§6.1), irregular patterns are not (Bercovici *et al.* 1989*a, b*). Thus not only are the regular polyhedral patterns preferred at the onset of convection (Busse 1975; Busse

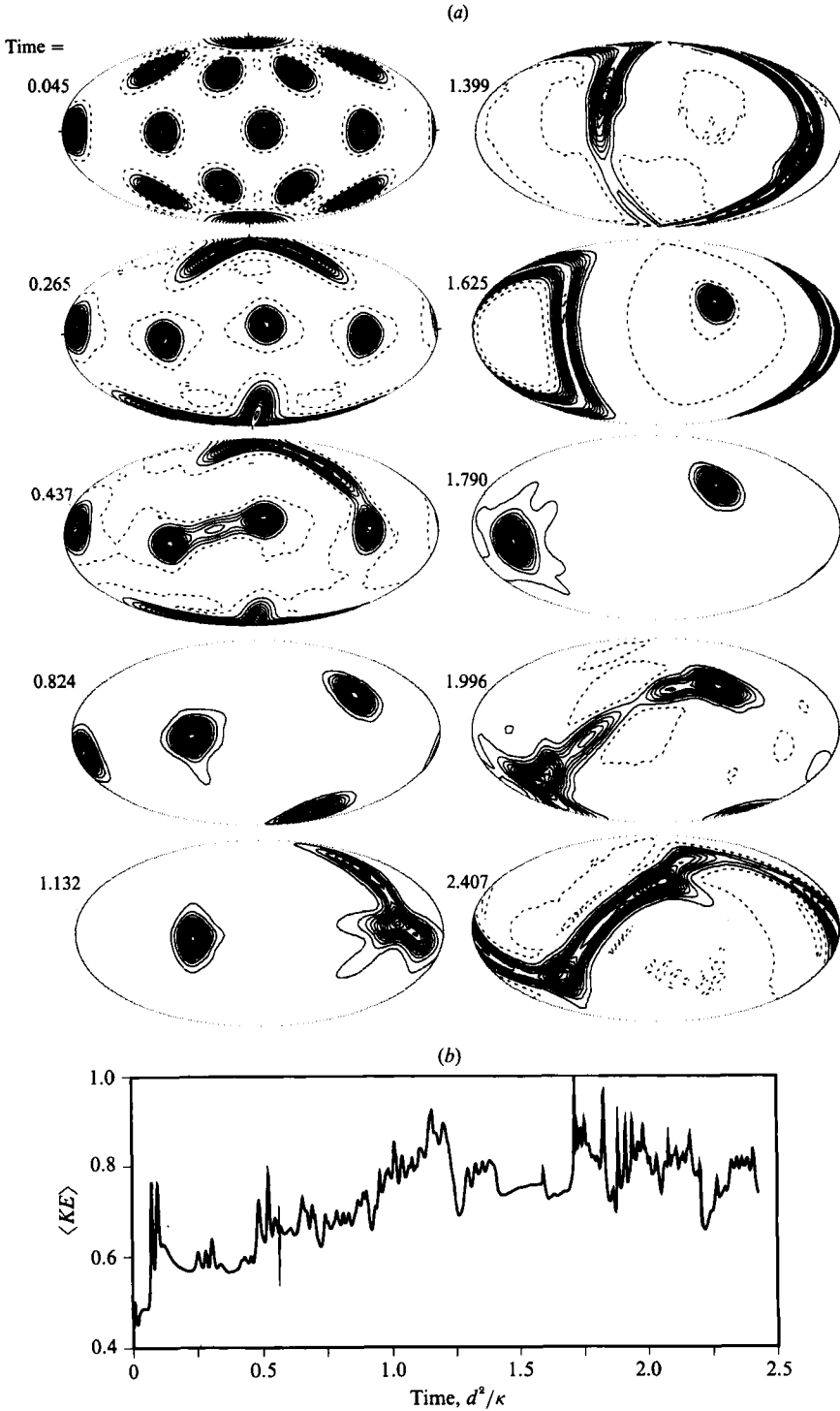


FIGURE 10. Time dependence for the case with  $\langle Ra \rangle = 16000$ ,  $\overline{Di} = 0.5$  and  $T_{\text{bot}}/\Delta T_{\text{sa}} = 10$ . (a) Contours of radial velocity (at mid-depth) for different times. Solid contours denote positive radial velocity and dashed contours denote negative radial velocity. See table 6 for contouring information. (b) Volume-averaged kinetic energy  $\langle KE \rangle$  versus time.

Time	0.045	0.125	0.265	0.335	0.437	0.525	0.731
$v_{\min}$	-34.62	0	-20.19	0	-20.19	-23.08	-23.08
$v_{\max}$	259.65	375.05	282.73	375.05	282.73	375.05	346.20
$\Delta v_r$	17.31	25.96	20.19	25.96	20.19	23.08	23.08

TABLE 6. Same as table 5, but for figure 10(a)

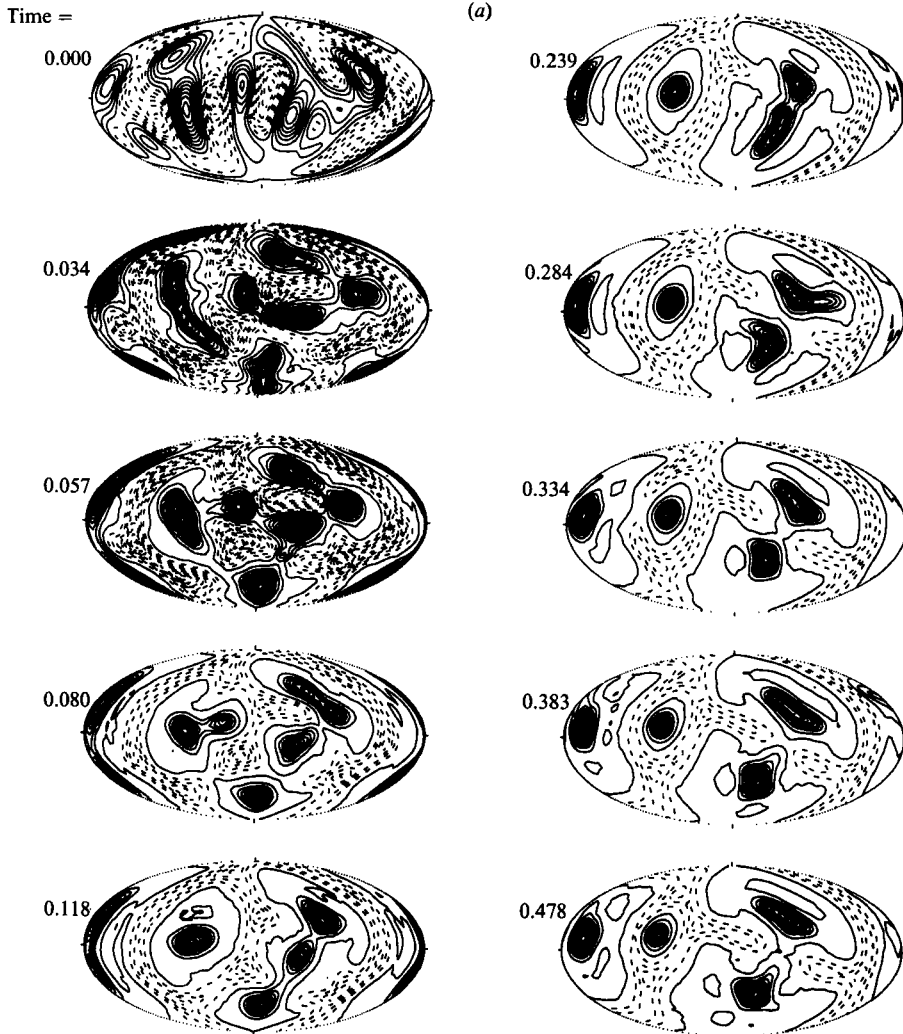


FIGURE 11(a). For caption see facing page.

& Riahi 1982), but they are stable in the strongly nonlinear regime. Irregular patterns generated by random initial conditions, on the other hand, lead to time-dependent solutions whose patterns are not always related to the least stable modes at the onset of convection, as are the regular polyhedral patterns.

In this subsection we simulate convection with irregular convective patterns (by starting the simulations with random initial conditions). To test the influence of

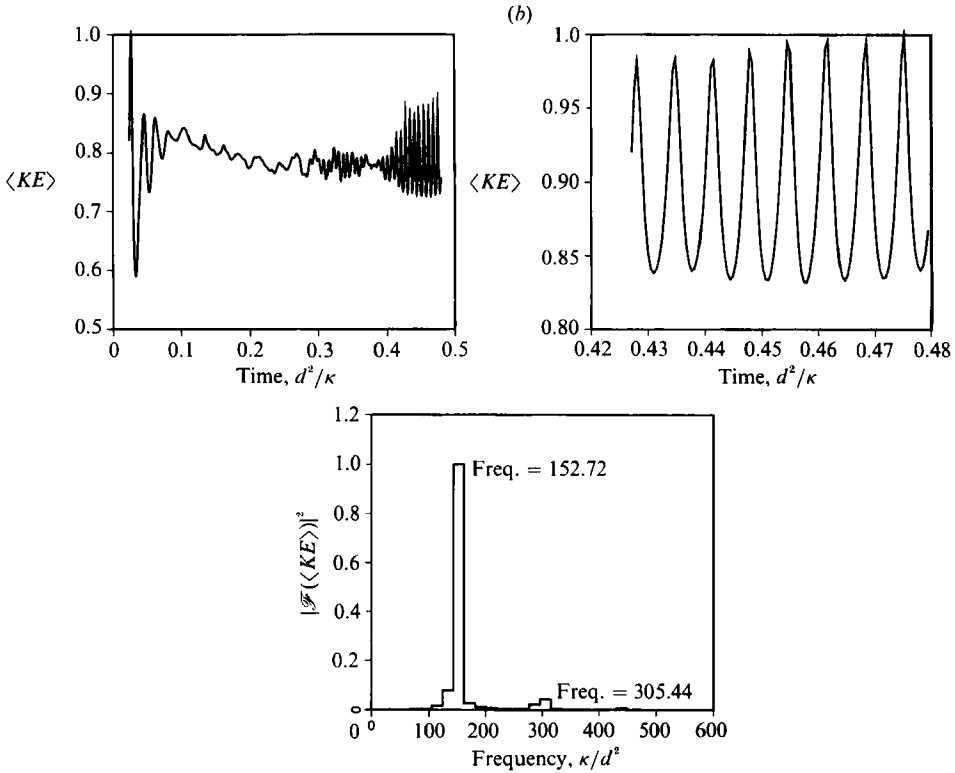


FIGURE 11. Time-dependent behaviour of convection for the case with random initial conditions,  $\langle Ra \rangle = 100 \langle Ra \rangle_{cr}$  and  $Di = 0$ . (a) See caption to figure 10(a) and table 7 for contouring information. (b) Volume-averaged kinetic energy  $\langle KE \rangle$  versus time and the corresponding Fourier power spectrum for  $0.42 \leq t \leq 0.48$ .

Time	0	0.034	0.057	0.080	0.118
$v_{rmin}$	-92.32	-288.50	-317.35	-288.50	-230.80
$v_{rmax}$	103.86	490.45	577.00	634.70	634.70
$\Delta v_r$	11.54	28.85	28.85	57.70	57.70
Time	0.239	0.334	0.383	0.478	
$v_{rmin}$	-173.10	-173.10	-173.10	-173.10	
$v_{rmax}$	692.40	750.10	807.80	750.10	
$\Delta v_r$	57.70	57.70	57.70		

TABLE 7. Same as table 5, but for figure 11(a)

compressibility on the pattern evolution and temporal behaviour of these solutions, we carry out two simulations, for  $\overline{Di} = 0$  and 0.5, with identical initial conditions. Since we are comparing the temporal behaviour of the two cases, the Rayleigh numbers are set exactly equal to  $100 \langle Ra \rangle_{cr}$ . Other parameter values are identical to those in the cases with  $\overline{T}_{bot}/\Delta T_{sa} = 1$  that were previously discussed. These solutions have truncation levels  $N = 18$  and  $L = 31$ . The power spectra of one of the solutions are shown in figure 2(a). After the first 1000 time steps (or  $0.03\tau_{diff}$ ) of the simulations, the pattern evolution for the two cases already diverges (figures 11, 12).

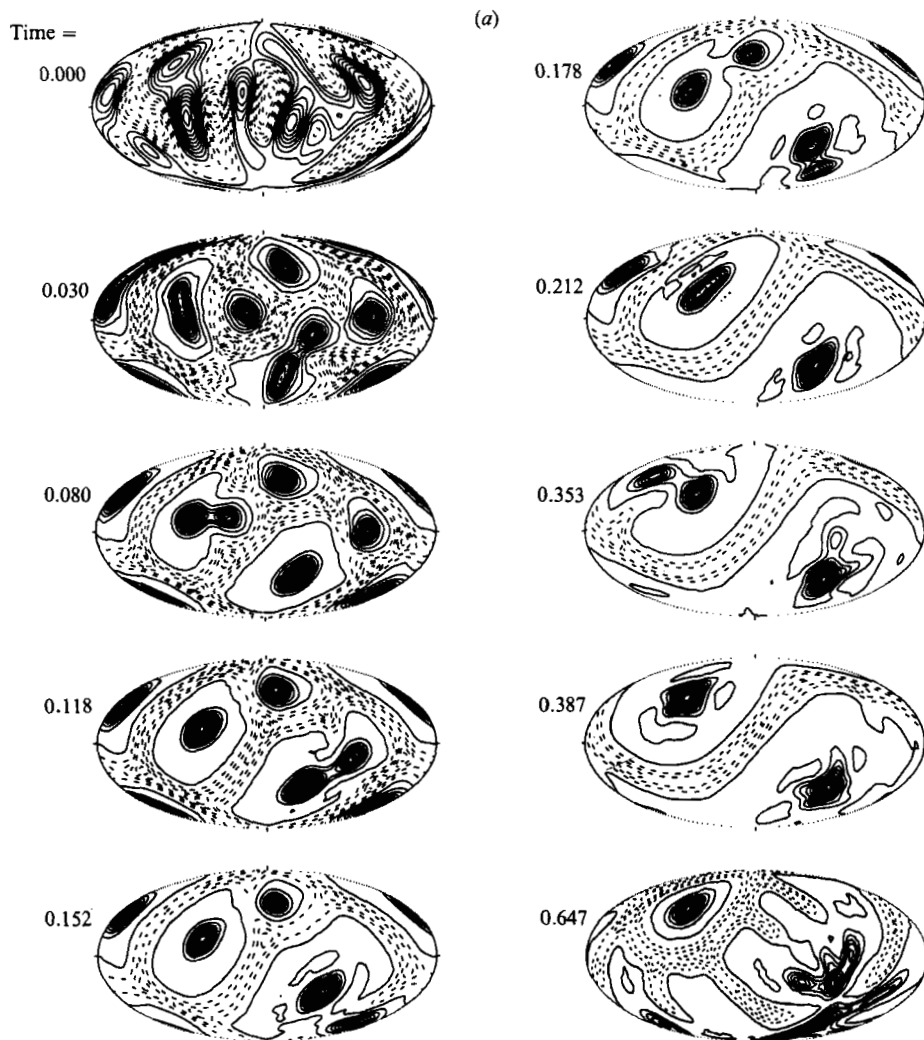


FIGURE 12(a). For caption see facing page.

The upwellings in the compressible case coalesce into separate plumes faster than in the Boussinesq case. At  $t = 0.08$  both cases have the same number of plumes, and by  $t \approx 0.23$ , both cases are evolving toward a three-plume configuration. However, by  $t = 0.284$ , the fusion of two plumes in the  $\overline{Di} = 0$  case has stalled and the pattern settles into a four-plume configuration for the remainder of the simulation.

The  $\overline{Di} = 0.5$  case continues its fusion of plumes until reaching the three-plume configuration by  $t \approx 0.2$ . This planform lasts for a very long time (from  $t = 0.19$  to  $t = 0.34$ ) until it becomes unstable and collapses into a two-plume pattern. This two-plume pattern persists for the remainder of the calculation although the plume in the southern hemisphere undergoes continuous instabilities as it breaks up and recombines. The plume in the northern hemisphere is, by comparison, very stable. The two-plume planform is a fairly robust solution for compressible convection at these  $\langle Ra \rangle$ , having been obtained elsewhere with different initial conditions (Bercovici *et al.* 1989*a, b*; Schubert *et al.* 1990).

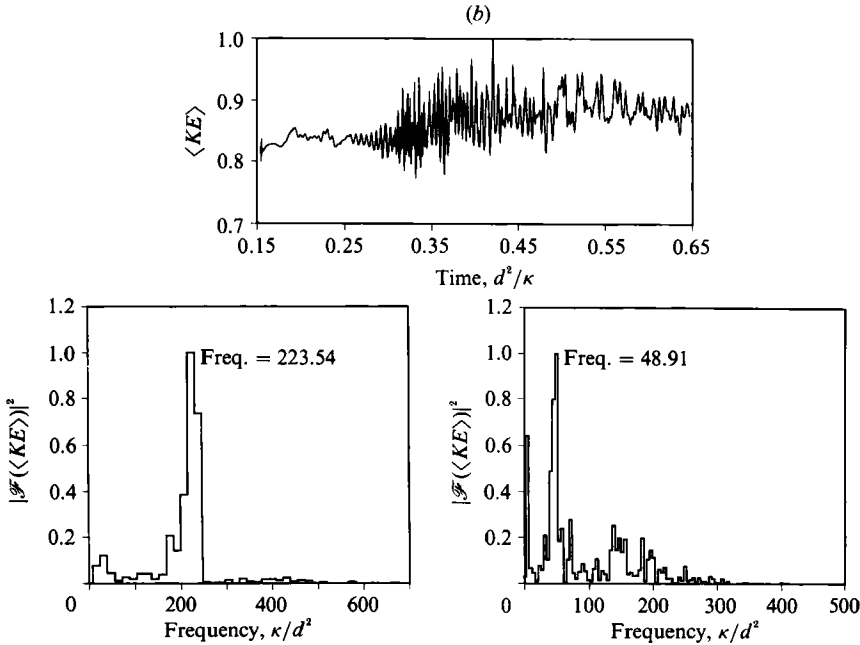


FIGURE 12. Time-dependent behaviour of convection for the case with random initial conditions,  $\langle Ra \rangle = 100 \langle Ra \rangle_{cr}$  and  $\overline{Di} = 0.5$ . (a) See caption to figure 10(a) and table 8 for contouring information. (b) Volume-averaged kinetic energy  $\langle KE \rangle$  versus time and the corresponding Fourier power spectrum for two different sequences of the  $\langle KE \rangle$  time series:  $0.35 \leq t \leq 0.40$  (left) and  $0.50 \leq t \leq 0.65$  (right).

Time	0.030	0.080	0.118	0.152	0.178	0.315	0.353	0.387
$v_{rmin}$	-519.30	-346.20	-288.50	-259.65	-259.65	-259.65	-259.65	-259.65
$v_{rmax}$	692.40	923.20	980.90	1125.15	1038.60	1125.15	1038.60	1038.60
$\Delta v_r$	57.70	57.70	57.70	86.55	86.55	86.55	86.55	86.55

TABLE 8. Same as table 5, but for figure 12(a)

The dominant spherical harmonic modes for both cases decrease in wavenumber throughout their pattern evolutions, as is evident by the reduction in the number of upwelling plumes. The dominant mode for the initial condition is the  $l = 6, m = 6$  mode, with several other large sectoral modes (at  $l = m = 2, 3$  and  $4$ ). At the last time step, the dominant mode for the  $\overline{Di} = 0$  case is at  $l = 3, m = 1$  when measured by the entropy variance and at  $l = 2, m = 2$  for the kinetic energy. Normally the dominant modes for entropy variance and kinetic energy coincide. However, near the end of the simulation, a small plume begins to grow near the south pole; this plume affects the thermal field but it has not yet gathered enough buoyancy to affect the velocity field. For  $\overline{Di} = 0.5$ , the dominant mode at the end of the simulation is at  $l = 2, m = 1$  (evident in the pattern with the two plumes residing in diagonal quadrants of the sphere).

The evolution of the kinetic energy for both cases is characterized by small-amplitude irregular oscillations while the patterns evolve to their final configuration, after which large-amplitude (with 20% variations in  $\langle KE \rangle$ ) oscillations occur (figures 11b, 12b). The  $\langle KE \rangle$  for the  $\overline{Di} = 0$  case settles into a singly periodic

oscillation in the last portion of the calculation. The  $\langle KE \rangle$  for the  $\overline{Di} = 0.5$  case is strongly periodic once it has reached the two-plume pattern, especially between  $t = 0.35$  and  $t = 0.4$ ; however, the oscillation appears to develop a low-frequency modulation once the southern plume begins its erratic behaviour ( $t \geq 0.5$ ). It is worth noting that while the solutions undergo their major transformations, the global kinetic energy is relatively quiescent, and after the solutions have (probably) reached a final state, the kinetic energy is very time dependent. This may occur because while the patterns are still changing there is not enough time for oscillations in the pattern to establish a resonance with the convective overturn cycle. This hypothesis is supported by the fact that the frequency of the  $\langle KE \rangle$  oscillations in the strongly variable regimes of the time series is commensurate with the overturn frequencies.

The most significant difference between the two cases with  $\overline{Di} = 0$  and  $0.5$  is that the final pattern of the Boussinesq case has more upwelling plumes than the final pattern of the anelastic-compressible case. This may occur because adiabatic and viscous heating in the compressible case weaken downwellings and thus facilitate plume fusion. For example, as two plumes begin to coalesce, the downwelling region between them becomes highly sheared, creating more viscous heating which then warms and weakens the downwelling, thus enhancing plume fusion.

The Nusselt number for the  $\overline{Di} = 0$  case varies in time between 6.3 and 6.6. The  $Nu$  for  $\overline{Di} = 0.5$  varies between 4.9 and 5.1. These compare to  $Nu = 6.7$  and  $Nu = 5.5$  for the  $\overline{Di} = 0$  and  $0.5$  cases with  $\langle Ra \rangle = 80000$  that are steady and have tetrahedral patterns. Even accounting for the difference in  $\langle Ra \rangle$ , the time-dependent cases have slightly poorer heat transport efficiencies than the steady, tetrahedral solutions.

## 7. Discussion

### 7.1. Penetrative convection and time dependence

In this study, we found that convection becomes time dependent at fairly low Rayleigh numbers when  $\overline{T}_{\text{bot}}/\Delta T_{\text{sa}}$  is large (§§5.5 and 6.2). The large values of  $\overline{T}_{\text{bot}}/\Delta T_{\text{sa}}$  correspond to penetrative convection with the upper portion of the spherical shell stable and the upper boundary layer essentially eliminated. Time dependence also occurs in compressible convection when the lower boundary layer is eliminated (Jarvis & McKenzie 1980; Machetel & Yuen 1989). In addition, time dependence is known to occur in purely internally heated convection with an insulated lower boundary (thus, no lower boundary layer) at Rayleigh numbers well below those for purely basally heated convection (Carrigan 1985). These results imply that elimination of one boundary layer in convection leads to a greater likelihood of time-dependent behaviour. A possible explanation for this is that vertical currents have greater freedom to drift when there is only a single boundary layer (since they drift through a weak background of return flow).

### 7.2. Cylindrical upwellings and planar downwellings

A fundamental question concerning three-dimensional spherical convection is why upwelling occurs in cylindrical plumes surrounded by a network of planar sheet-like downwellings for a wide range of compressibilities and heating modes (Bercovici *et al.* 1989*a, b, c*). In plane-layer basally heated convection with a three-dimensional cell structure (e.g. hexagonal or spoke pattern), the upwelling and downwelling currents appear sheet-like as they emanate from the bottom or top boundary (Whitehead & Parsons 1978; Houseman 1988; Travis, Olson & Schubert 1990; Weinstein & Olson 1990). These up- and downwelling sheets appear to intersect midway through the

layer where they cut each other into segments which coalesce into plumes; thus upwelling is sheet-like in the lower half of the layer, and plume-like in the upper half (and vice versa for downwellings). However, spherical geometry should influence where the upwelling and downwelling sheets intersect. The radius at which upwelling and downwelling sheets intersect can be estimated by balancing the buoyancy forces on two sheets, one sinking and one rising. As a first approximation, we assume the sheets have equal horizontal thickness, extend horizontally an angle  $\phi$  (such that the horizontal length of either sheet at a radius  $r$  is  $\phi r$ ), and that their density anomalies are nearly constant in radius. With these assumptions, the balance of the two sheets' net buoyancy leads to

$$\bar{\rho}'_u(r_c^2 - r_{\text{bot}}^2) = \bar{\rho}'_d(r_{\text{top}}^2 - r_c^2), \quad (7.1)$$

where  $\bar{\rho}'_u$  and  $\bar{\rho}'_d$  are, respectively, the horizontally averaged density anomalies of the upwelling and downwelling sheets,  $r_c$  is the radius at which the sheets intersect and gravity is assumed constant (as it very nearly is in the Earth's mantle and in this numerical model). Equation (7.1) is merely a balance of the mass anomaly per unit thickness of the two sheets. If the boundary layers are of equal thickness, then by conservation of energy  $\Delta T_{\text{bot}} r_{\text{bot}}^2 = \Delta T_{\text{top}} r_{\text{top}}^2$ , where  $\Delta T_{\text{bot}}$  and  $\Delta T_{\text{top}}$  are the temperature drops across the bottom and top boundary layers. Since  $\bar{\rho}'_u$  and  $\bar{\rho}'_d$  are proportional to  $\Delta T_{\text{bot}}$  and  $\Delta T_{\text{top}}$ , respectively, then  $\bar{\rho}'_u \approx (r_{\text{top}}/r_{\text{bot}})^2 \bar{\rho}'_d$  and we obtain

$$r_c^2 \approx \frac{2r_{\text{top}}^2}{1 + (r_{\text{top}}/r_{\text{bot}})^2}. \quad (7.2)$$

If  $r_{\text{bot}} = r_{\text{top}} - \epsilon$ , then, to second order in  $\epsilon$ ,  $r_c = \frac{1}{2}(r_{\text{top}} + r_{\text{bot}}) - \frac{3}{8}(\epsilon/r_{\text{top}})^2$ ; in the limit of  $\epsilon/r_{\text{top}} \ll 1$ ,  $r_c$  is midway through the shell, which is the plane-layer result. Equation (7.2) thus implies that  $r_c$  is always less than the radius midway through the shell. The effect of the spherical geometry is to move the level at which upwelling and downwelling sheets cut each other into plumes closer to the bottom boundary. Therefore, upwelling will be plume-like and downwellings sheet-like throughout most of the shell. When  $r_{\text{bot}}/r_{\text{top}} = 0.547$ , as in this study,  $r_c/r_{\text{top}} = 0.68$ , which is about 70% of the distance to the bottom boundary from the top. However, in this study, upwelling is never in the form of sheets and emanates as plumes from the bottom boundary; this implies that there are additional effects causing  $r_c \leq r_{\text{bot}}$ . The additional effects may arise from the focusing and defocusing influences of the concave upper and convex lower boundaries (Bercovici *et al.* 1989c).

When internal heating is included, the top boundary layer will have a larger temperature drop than in the purely basally heated case. Thus, the downwelling sheet will have a greater density anomaly, which will move  $r_c$  away from the bottom boundary (since the downwelling sheet will need less volume to balance the buoyancy of the upwelling sheet). This is found to occur in numerical simulations (Glatzmaier *et al.* 1990).

The formation of plumes probably occurs because the points where the upwelling and downwelling sheets intersect are areas of high pressure, while those regions of the sheets that do not intersect have lower pressure. Thus, the upwelling is forced into narrow currents at the resulting pressure minima.

### 7.3. Geophysical discussion

The effects of compressibility on mantle convection are most significant when the net superadiabatic temperature drop is small relative to the characteristic adiabatic temperature, i.e. when  $\bar{T}_{\text{bot}}/\Delta T_{\text{sa}} \sim O(10)$ . For the Earth, the net superadiabatic

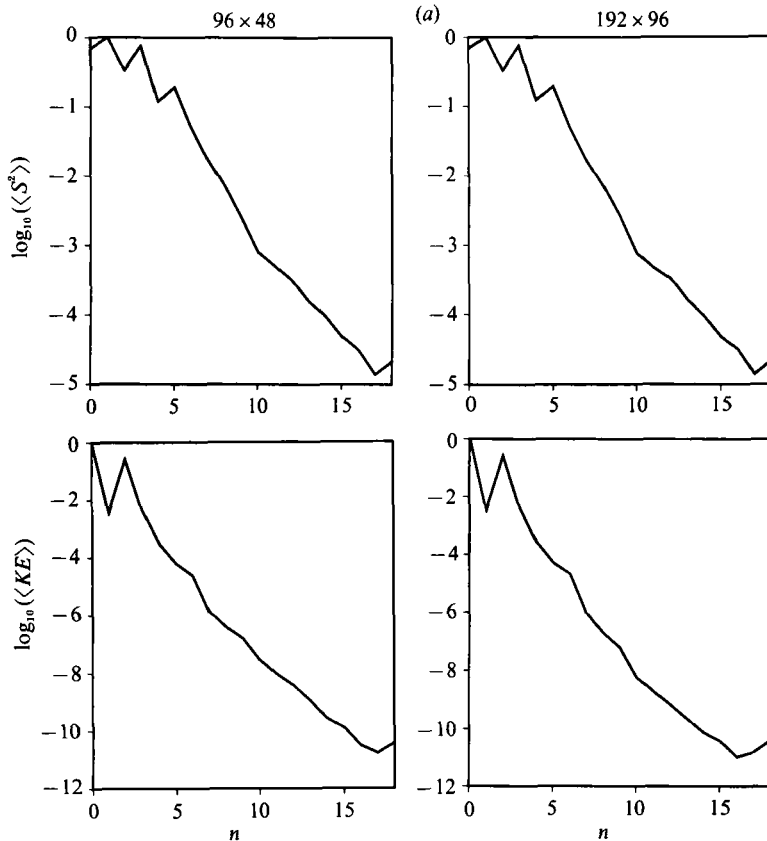


FIGURE 13(a). For caption see facing page.

temperature drop (i.e. the sum of the temperature drops across the thermal boundary layers in the mantle) is of the same order as the temperature at the base of the mantle adiabat; i.e. for the Earth's mantle  $\bar{T}_{\text{bot}}/\Delta T_{\text{sa}} \sim O(1)$ . Thus, compressibility is probably not of great importance in determining the spatial structure of mantle convection. Yet, as shown in §6.3, compressibility does affect the temporal behaviour of convection.

This study does not include the effects of internal heating which is the primary heat source for terrestrial mantles (Turcotte & Schubert 1982). The main influence of compressibility on convection when internal heating is present is to cause penetrative convection near the base of the shell (Machetel & Yuen 1989). This occurs because, as the proportion of internal heating increases (while the total heat flow remains fixed), the basal heat flow decreases and eventually becomes smaller than the conductive heat flow along the adiabat, causing the fluid near the base of the shell to become subadiabatic. However, whether this actually occurs in the Earth's mantle can be easily estimated by comparing the heat flow emanating from the core to the conductive heat flow along the adiabat at the core-mantle boundary. The core heat flow is approximately  $20 \text{ mW/m}^2$  (Stevenson *et al.* 1983). The conductive heat flow along the adiabat at the core-mantle boundary is  $\kappa \alpha g T / c_p$ , evaluated at the base of the mantle; this value is about  $1 \text{ mW/m}^2$ . Thus, mantle fluid near the core-mantle boundary is highly superadiabatic and penetrative convection probably does not occur in the Earth's mantle.

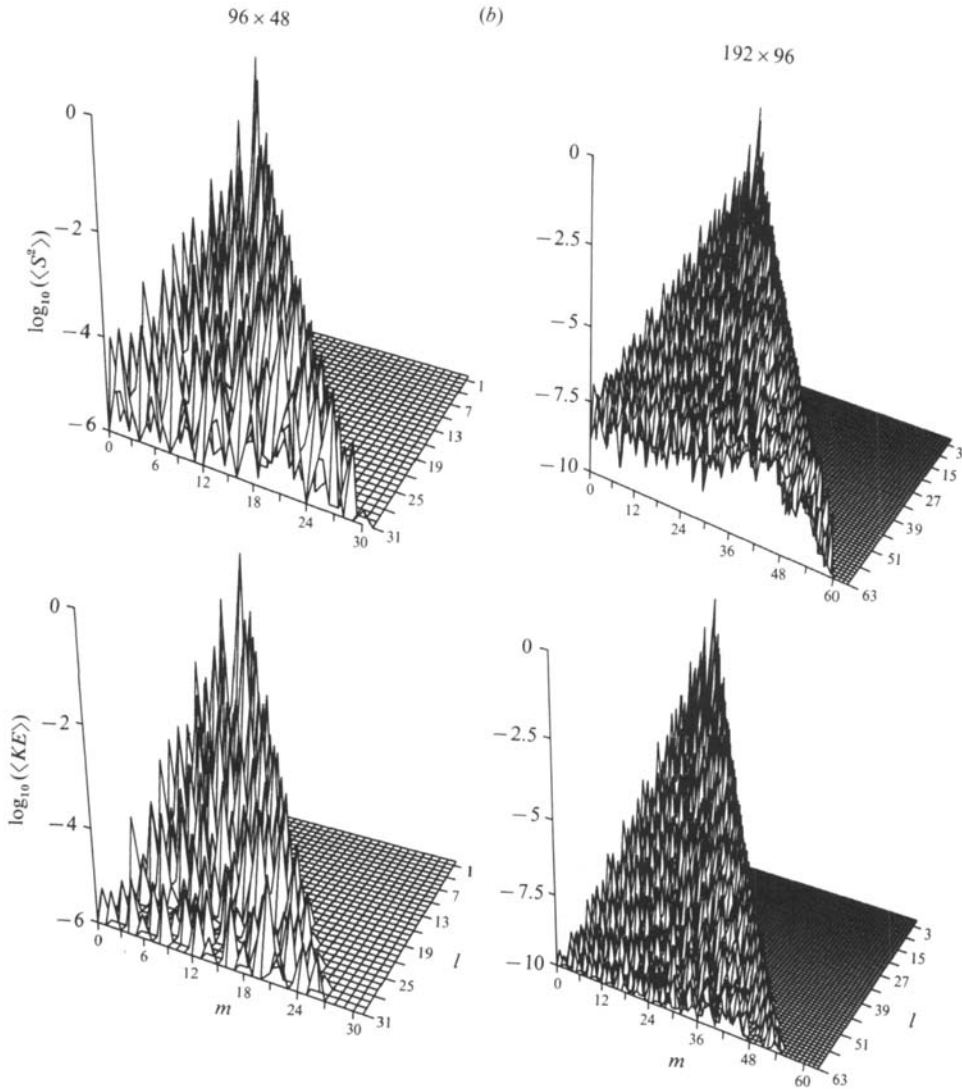


FIGURE 13. Power spectra for (a) the Chebyshev and (b) spherical harmonic expansions for the low and high resolution cases of the Appendix. The low resolution case has 96 longitudinal and 48 latitudinal grid points and is referred to in the figure as  $96 \times 48$ ; the high resolution case has 192 longitudinal and 96 latitudinal grid points and is referred to as  $192 \times 96$ . The power spectra for both the entropy variance and kinetic energy are shown.

Previous studies of compressible convection (Jarvis & McKenzie 1980; Machetel & Yuen 1989) have concluded that mantle compressibility can stabilize the lower portion of the mantle, causing penetrative convection there and effectively precluding upwelling plumes. However, as shown in this paper, the opposite scenario is also possible wherein the upper part of the fluid layer is stabilized and narrow downwelling currents are eliminated. The results of the previous studies are influenced by their use of a constant dissipation number. A constant  $Di$  leads to a very steep adiabat at the base of the fluid layer, and thus increases the chances of penetrative convection occurring near the base of the layer. For example, in the axisymmetric spherical shell study (Machetel & Yuen 1989), the use of a constant  $Di$

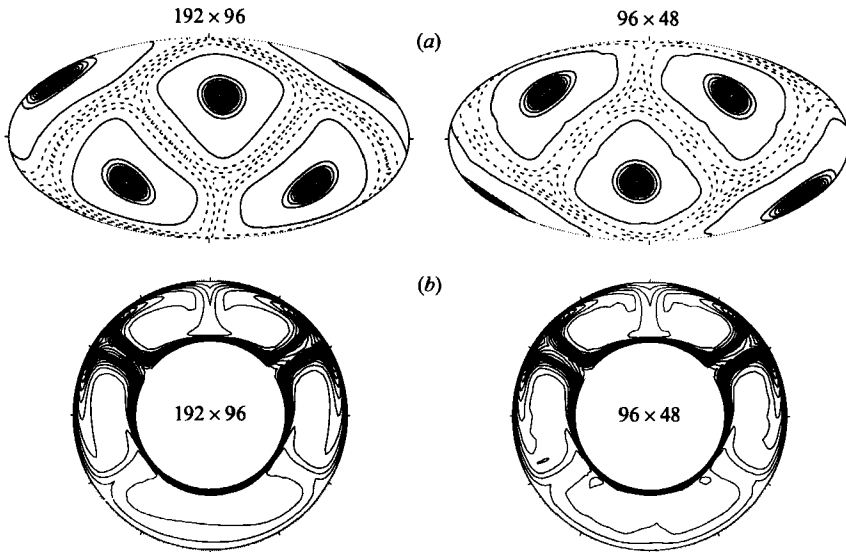


FIGURE 14. Velocity and thermal fields for the two cases of figure 13. (a) Radial velocity contours at mid-depth ( $r/r_{\text{top}} = 0.77$ ). Solid contours denote positive radial velocity and dashed contours denote negative radial velocity. The minimum and maximum contour values and the contour interval are, respectively,  $-240$ ,  $1000$  and  $80$ , for both cases. (b) Total entropy contours in a meridional plane. The minimum and maximum contour values and the contour interval are, respectively,  $-0.35$ ,  $0.77$  and  $0.07$ , for both cases.

causes penetrative flow to occur at an unrealistically low internal heating rate due to the exaggerated steepness of the adiabat at the base of the shell. When a more realistic adiabat is employed, penetrative flow does not occur unless the super-adiabatic temperature drop is unreasonably small for the Earth; even when internal heating is included, penetrative convection does not readily occur so long as the adiabat is Earth-like (Solheim & Peltier 1990).

In general, compressibility in mantle convection is important if the conductive heat flow along the adiabat is comparable with the total heat flow through the mantle. However, both heat flows increase as the size of the planet and its mantle increase. While a large terrestrial planet (e.g. Earth) is likely to cause greater compression of its mantle than a smaller planet (e.g. Mars), it will also cool more slowly than a smaller planet. (A large planet is also more likely to initiate freezing of an inner core because of higher central pressures (Stevenson *et al.* 1983), and this is another heat source by virtue of latent heat release.) Therefore, while a large planet is most likely to undergo significant compression, it is also likely to be hotter and thus have larger heat flow, which diminishes the significance of compressibility.

The authors wish to acknowledge helpful comments from two anonymous reviewers and discussions with P. H. Roberts, U. R. Christensen and participants of the Los Alamos National Laboratory (LANL) Mantle Convection Workshop. A large part of this work comprised a portion of the first author's doctoral thesis while he was at UCLA and was supported by grant NAG5152 from NASA, a grant from the Institute of Geophysics and Planetary Physics at LANL, and a computing grant from the San Diego Supercomputer Center (SDSC). Revisions were supported by the W. M. Keck Geodynamics program during the first author's postdoctoral fellowship at the Woods Hole Oceanographic Institution, and by the University of Hawaii.

Computations and graphics were generated on a CRAY X-MP-48 and a CRAY Y-MP-864 at SDSC. A portion of the calculations for the appendix were performed on a CRAY Y-MP-832 at LANL.

### Appendix. Convergence test for horizontal resolution

A convergence test has been carried out to examine the accuracy of the spherical harmonic expansions used in this study. A steady solution with a tetrahedral pattern and  $\langle Ra \rangle = 80000$ ,  $\overline{Di} = 0.5$  and  $\overline{T}_{\text{bot}}/\Delta T_{\text{sa}} = 1$  has been calculated with two resolutions, one with 96 longitudinal grid points, 48 latitudinal Gaussian quadrature points and 37 Chebyshev collocation grid points in radius, and the other with twice the number of grid points in latitude and longitude.

The Chebyshev and spherical harmonic power spectra (for both entropy variance and kinetic energy) are shown in figure 13 for both the lower and higher resolution cases. The Chebyshev power spectra are essentially identical in both cases. The spherical harmonic power spectrum of the higher resolution case drops nearly eight orders of magnitude for the entropy variance and almost ten orders of magnitude for the kinetic energy, nearly twice that of the lower resolution case. The higher resolution case is, therefore, highly resolved.

Figure 14 shows plots of radial velocity midway through the shell and entropy along a meridional plane for both the higher and lower resolution cases. The radial velocity and entropy fields of the two cases are virtually identical except for some small-scale features that appear in the lower resolution case. The maximum upwelling velocities of the two cases differ by between 0 and 0.1% and the maximum downwelling velocities differ by between 0 and 0.3%. The maximum upwelling entropy anomalies midway through the shell for the two cases differ between 4 and 5%; the downwelling entropy anomalies differ between 0.5 and 1.5%. The greater discrepancy in the entropy field occurs because the thermal field is harder to resolve in the limit of infinite  $Pr$ , and the entropy extrema are very small-scale features. Therefore, the spectral expansions used elsewhere in this paper are very good at resolving the flow field and are adequate for resolving the large- and medium-scale features of the thermal field. As the resolution of a simulation is improved, some spurious small-scale features are smoothed out.

Though the solution for the lower resolution case has finer resolution in radius (especially near the boundaries) than horizontally, the upwelling plumes are well resolved and naturally thicker than the horizontal boundary layers. The two frames of figure 14(b) can be superimposed to show that the thickness of the boundary layers and upwelling plumes are unchanged at double the horizontal resolution. The greater thickness of the upwelling plumes occurs because fluid in the upwelling plume is moving along a line in the meridional plane while most of the fluid in the horizontal boundary layers is out of the meridional plane.

### REFERENCES

- BATCHELOR, G. K. 1967 *An Introduction to Fluid Dynamics*. Cambridge University Press.
- BAUMGARDNER, J. R. 1985 Three-dimensional treatment of convective flow in the Earth's mantle. *J. Statist. Phys.* **39**, 501–511.
- BAUMGARDNER, J. R. 1988 Application of supercomputers to 3-d mantle convection. In *The Physics of the Planets* (ed. S. K. Runcorn), pp. 199–231. John Wiley.
- BERCOVICI, D. 1989 A numerical investigation of thermal convection in highly viscous spherical

shells with applications to mantle dynamics in the Earth and other terrestrial planets. Ph.D. dissertation, University of California, Los Angeles.

- BERCOVICI, D., SCHUBERT, G. & GLATZMAIER, G. A. 1989*a* Three-dimensional spherical models of convection in the Earth's mantle. *Science* **244**, 950–955.
- BERCOVICI, D., SCHUBERT, G. & GLATZMAIER, G. A. 1989*b* Influence of heating mode on three-dimensional mantle convection. *Geophys. Res. Lett.* **16**, 617–620.
- BERCOVICI, D., SCHUBERT, G. & GLATZMAIER, G. A. 1991 Modal growth and coupling in three-dimensional spherical convection. *Geophys. Astrophys. Fluid Dyn.* **61**, 149–159.
- BERCOVICI, D., SCHUBERT, G., GLATZMAIER, G. A. & ZEBIB, A. 1989*c* Three-dimensional thermal convection in a spherical shell. *J. Fluid Mech.* **206**, 75–104.
- BERCOVICI, D., SCHUBERT, G. & ZEBIB, A. 1988 Geoid and topography for infinite Prandtl number convection in a spherical shell. *J. Geophys. Res.* **93**, 6430–6436.
- BUSSE, F. H. 1975 Patterns of convection in spherical shells. *J. Fluid Mech.* **72**, 67–85.
- BUSSE, F. H. & RIAHI, N. 1982 Patterns of convection in spherical shells. Part 2. *J. Fluid Mech.* **123**, 283–301.
- BUSSE, F. H. & RIAHI, N. 1988 Mixed-mode patterns of bifurcations from spherically symmetric basic states. *Nonlinearity* **1**, 379–388.
- CARRIGAN, C. R. 1985 Convection in an internally heated, high Prandtl number fluid: A laboratory study. *Geophys. Astrophys. Fluid Dyn.* **32**, 1–21.
- CHANDRASEKHAR, S. 1939 *An Introduction to the Study of Stellar Structure*. University of Chicago Press.
- CHANDRASEKHAR, S. 1961 *Hydrodynamic and Hydromagnetic Stability*. Oxford University Press.
- DZIEWONSKI, A. M. 1984 Mapping the lower mantle: Determination of lateral heterogeneity in  $P$  velocity up to degree and order 6. *J. Geophys. Res.* **89**, 5929–5952.
- DZIEWONSKI, A. M. & ANDERSON, D. L. 1981 Preliminary reference earth model (PREM). *Phys. Earth Planet. Inter.* **25**, 297–356.
- DZIEWONSKI, A. M. & WOODHOUSE, J. H. 1987 Global images of the earth's interior. *Science* **236**, 37–48.
- GLATZMAIER, G. A. 1984 Numerical simulations of stellar convective dynamos I. The model and method. *J. Comput. Phys.* **55**, 461.
- GLATZMAIER, G. A. 1988 Numerical simulations of mantle convection: time-dependent, three-dimensional, compressible, spherical shell. *Geophys. Astrophys. Fluid Dyn.* **43**, 223–264.
- GLATZMAIER, G. A., SCHUBERT, G. & BERCOVICI, D. 1990 Chaotic subduction-like downflows in a spherical model of convection in the Earth's mantle. *Nature* **347**, 274–277.
- GOUGH, D. O. 1969 The anelastic approximation for thermal convection. *J. Atmos. Sci.*, **26**, 448–456.
- GRAHAM, E. 1975 Numerical simulation of two-dimensional compressible convection. *J. Fluid Mech.* **70**, 689–703.
- HAGER, B. H., CLAYTON, R. W., RICHARDS, M. A., COMER, R. P. & DZIEWONSKI, A. M. 1985 Lower mantle heterogeneity, dynamic topography, and the geoid. *Nature* **313**, 541–545.
- HART, J. E., GLATZMAIER, G. A. & TOOMRE, J. 1986*a* Space laboratory and numerical simulations of thermal convection in a rotating hemispherical shell with radial gravity. *J. Fluid Mech.* **173**, 519–544.
- HART, J. E., TOOMRE, J., DEANE, A. E., HURLBURT, N. E., GLATZMAIER, G. A., FICHTL, F., LESLIE, F., FOWLIS, W. W. & GILMAN, P. A. 1986*b* Laboratory experiments on planetary and stellar convection performed on Spacelab 3. *Science* **234**, 61.
- HEWITT, J. M., MCKENZIE, D. P. & WEISS, N. O. 1975 Dissipative heating in convective flows. *J. Fluid Mech.* **68**, 721–738.
- HOUSEMAN, G. 1988 The dependence of convection planform on mode of heating. *Nature* **332**, 346–349.
- HSUI, A. T., TURCOTTE, D. L. & TORRANCE, K. E. 1972 Finite amplitude thermal convection within a self-gravitating fluid sphere. *Geophys. Fluid Dyn.* **3**, 35–44.
- JARVIS, G. T. & MCKENZIE, D. P. 1980 Convection in a compressible fluid with infinite Prandtl number. *J. Fluid Mech.* **96**, 515–583.
- KAULA, W. M. 1990 Venus: A contrast in evolution to Earth. *Science* **247**, 1191–1196.

- KROGER, P. M., LYZENGA, A., WALLACE, K. S. & DAVIDSON, J. M. 1987 Tectonic motion in the western United States inferred from very long baseline interferometry measurements, 1980–1986. *J. Geophys. Res.* **92**, 14151–14163.
- MACHETEL, P. & RABINOWICZ, M. 1985 Transitions to a two mode axisymmetrical spherical convection: Application to the Earth's mantle. *Geophys. Res. Lett.* **12**, 227–231.
- MACHETEL, P., RABINOWICZ, M. & BERNADET, P. 1986 Three-dimensional convection in spherical shells. *Geophys. Astrophys. Fluid Dyn.* **37**, 57–84.
- MACHETEL, P. & YUEN, D. A. 1986 The onset of time dependent convection in spherical shells as a clue to chaotic convection in the Earth's mantle. *Geophys. Res. Lett.* **13**, 1470–1473.
- MACHETEL, P. & YUEN, D. A. 1987 Chaotic axisymmetrical spherical convection and large-scale circulation. *Earth Planet. Sci. Lett.* **86**, 93.
- MACHETEL, P. & YUEN, D. A. 1988 Infinite Prandtl number spherical shell convection. In *Mathematical Geophysics* (ed. N. J. Vaar *et al.*), pp. 265–290. D. Reidel.
- MACHETEL, P. & YUEN, D. A. 1989 Penetrative convective flows induced by internal heating and mantle compressibility. *J. Geophys. Res.* **94**, 10609–10626.
- MINSTER, J. B. & JORDAN, T. H. 1978 Present-day plate motions. *J. Geophys. Res.* **83**, 5331–5354.
- MINSTER, J. B. & JORDAN, T. H. 1987 Vector constraints on western U.S. deformation from space geodesy, neotectonics, and plate motions. *J. Geophys. Res.* **92**, 4798–4804.
- MURNAGHAN, F. D. 1951 *Finite Deformation of an Elastic Solid*. John Wiley.
- OLSON, P. 1981 Mantle convection with spherical effects. *J. Geophys. Res.* **86**, 4881–4890.
- OLSON, P., SILVER, P. G. & CARLSON, R. W. 1990 The large-scale structure of convection in the Earth's mantle. *Nature* **344**, 209–215.
- OXBURGH, E. R. & TURCOTTE, D. L. 1978 Mechanisms of continental drift. *Rep. Prog. Phys.* **41**, 1249–1312.
- PELTIER, W. R. 1972 Penetrative convection in the planetary mantle. *Geophys. Fluid Dyn.* **5**, 47–88.
- QUARENI, F. & YUEN, D. A. 1988 Mean field methods in mantle convection. In *Mathematical Geophysics* (ed. N. J. Vaar *et al.*), pp. 227–264. D. Reidel.
- ROBERTS, P. H. 1987 Convection in spherical systems. In *Irreversible Phenomena and Dynamical Systems Analysis in Geosciences* (eds C. Nicolis & G. Nicolis). D. Reidel.
- RUNCORN, S. K. 1967 Flow in the mantle inferred from the low degree harmonics of the geopotential. *Geophys. J. R. Astron. Soc.* **14**, 375–384.
- SCHUBERT, G. 1979 Subsolidus convection in the mantles of the terrestrial planets. *Ann. Rev. Earth Planet. Sci.* **7**, 289–342.
- SCHUBERT, G., BERCOVICI, D. & GLATZMAIER, G. A. 1990 Mantle dynamics in Mars and Venus: Influence of an immobile lithosphere on three-dimensional mantle convection. *J. Geophys. Res.* **95**, 14105–14129.
- SCHUBERT, G., STEVENSON, D. & CASSEN, P. 1980 Whole planet cooling and the radiogenic heat source contents of the earth and moon. *J. Geophys. Res.* **85**, 2531–2538.
- SCHUBERT, G. & ZEBIB, A. 1980 Thermal convection of an internally heated infinite Prandtl number fluid in a spherical shell. *Geophys. Astrophys. Fluid Dyn.* **15**, 65.
- SILVER, P. G., CARLSON, R. W. & OLSON, P. 1988 Deep slabs, geochemical heterogeneity, and the large-scale structure of mantle convection: investigation of an enduring paradox. *Ann. Rev. Earth Planet. Sci.* **16**, 477–541.
- SOLHEIM, L. P. & PELTIER, W. R. 1990 Heat transfer and the onset of chaos in an axisymmetric anelastic model of whole mantle convection. *Geophys. Astrophys. Fluid Dyn.* **53**, 205–255.
- STACEY, F. D. 1977 *Physics of the Earth*. Wiley.
- STEINBACH, V., HANSEN, U. & EBEL, A. 1989 Compressible convection in the Earth's mantle: A comparison of different approaches. *Geophys. Res. Lett.* **16**, 633–636.
- STEVENSON, D. J., SPOHN, T. & SCHUBERT, G. 1983 Magnetism and thermal evolution of the terrestrial planets. *Icarus* **54**, 466–489.
- TRAVIS, B., OLSON, P. & SCHUBERT, G. 1990 The transition from two-dimensional to three-dimensional planforms in infinite-Prandtl-number thermal convection. *J. Fluid Mech.* **216**, 71–91.

- TURCOTTE, D. L., HSUI, A. T., TORRANCE, K. E. & SCHUBERT, G. 1974 Influence of viscous dissipation on Benard convection. *J. Fluid Mech.* **64**, 369–374.
- TURCOTTE, D. L. & SCHUBERT, G. 1982 *Geodynamics*. Wiley & Sons.
- WEINSTEIN, S. & OLSON, P. 1990 Planforms in thermal convection with internal heat sources at large Rayleigh and Prandtl numbers. *Geophys. Res. Lett.* **17**, 239–242.
- WHITEHEAD, J. A. & PARSONS, B. 1978 Observations of convection at Rayleigh numbers up to 760,000 in a fluid with large Prandtl number. *Geophys. Astrophys. Fluid Dyn.* **19**, 201–217.
- WOODHOUSE, J. H. & DZIEWONSKI, A. M. 1984 Mapping the upper mantle: Three dimensional modeling of earth structure by inversion of seismic wave-forms. *J. Geophys. Res.* **89**, 5953–5986.
- YOUNG, R. E. 1974 Finite-amplitude thermal convection in a spherical shell. *J. Fluid Mech.* **63**, 695–721.
- ZEBIB, A., GOYAL, A. K. & SCHUBERT, G. 1985 Convective motions in a spherical shell. *J. Fluid Mech.* **152**, 39–48.
- ZEBIB, A., SCHUBERT, G. & STRAUS, J. M. 1980 Infinite Prandtl number thermal convection in a spherical shell. *J. Fluid Mech.* **97**, 257.
- ZEBIB, A., SCHUBERT, G., DEIN, J. L. & PALIWAL, R. C. 1983 Character and stability of axisymmetric thermal convection in spheres and spherical shells. *Geophys. Astrophys. Fluid Dyn.* **23**, 1–42.